Thermodynamic description of the plutonium – α-D-isosaccharinic acid system I: Solubility, complexation and redox behavior

A. Tasi[a,*], X. Gaona[a,**], D. Fellhauer[a], M. Böttle[a], J. Rothe[a], K. Dardenne[a], R. Polly[a], M. Grivé[b], E. Colàs[b], J. Bruno[b], K. Källström[c], M. Altmaier[a], H. Geckeis[a]

[a] Karlsruhe Institute of Technology, Institute for Nuclear Waste Disposal, P.O. Box 3640, 76021, Karlsruhe, Germany
[b] Amphos21 Consulting S.L., Passeig de Garcia i Fària, 49-51, 1°-1a, E08019, Barcelona, Spain
[c] Svensk Kärnbränslehantering AB, Box 3091, SE-169 03, Solna, Sweden

ARTICLE INFO

Keywords:
Plutonium
Actinides
Isosaccharinic acid
Redox chemistry
Solubility
Thermodynamics

ABSTRACT

The impact of α-D-isosaccharinic acid (HISA), a degradation product of cellulose, on the solubility and redox behavior of hydrous Pu(IV) oxide was investigated from undersaturation conditions under Ar atmosphere in 0.1 m NaCl–NaOH–NaISA solutions. Redox conditions were buffered with hydroquinone (HQ) or Sn(II), resulting in ($pe + pH_m$) ≈ 9.0 and 1.5, respectively. The influence of ISA on Pu solubility was investigated as function of pH_m ($8 \leq pH_m \leq 13$) and ligand concentration (10^{-6} m ≤ $m(ISA)_{tot}$ ≤ 0.1 m).

In-situ X-ray diffraction and X-ray absorption spectroscopic measurements indicate that PuO_2(ncr,hyd) controls the solubility of Pu in all investigated systems. Presence of ISA poses an increase in plutonium solubility by up to 2.5 log-units. In HQ systems, slope analysis of solubility data in combination with solid phase characterization and density functional theory calculations resulted in chemical and thermodynamic models including the predominance of $Pu(IV)(OH)_3ISA_{-H}^-$ and $Pu(IV)(OH)_3ISA_{-2H}^{2-}$ complexes below and above $pH_m \approx 12$, respectively. In Sn(II) systems with $pH_m < 11.5$, a reductive dissolution occurs involving the formation of $Pu(III)(OH)ISA_{-H}$(aq). Experimental observations suggest also that Pu–ISA colloids importantly contribute to the overall Pu concentration in solution, both in HQ and Sn(II) systems. Although this process is not included in the thermodynamic model derived, it cannot be neglected for estimating Pu solubility limits under these conditions. This work provides the most comprehensive thermodynamic dataset available to date for the system Pu^{3+}–Pu^{4+}–OH^-–Cl^-–ISA^-–H_2O(l) valid under a wide range of conditions relevant for nuclear waste disposal.

1. Introduction

Underground repositories in stable geological formations are the internationally favoured option for the final disposal of nuclear waste. Strongly reducing conditions are expected to develop in the post-closure period of such facilities due to the anoxic corrosion of iron and steel. In the case of low and intermediate level waste (L/ILW), the preferred concept involves the use of cementitious materials for the stabilization of the waste and for construction purposes. The interaction of these materials with groundwater buffers the pH in the alkaline to hyperalkaline range ($10 \leq pH \leq 13.3$) over a very long time-scale. This concept and boundary conditions are also representative of SFR 1, the Repository for Short-lived Low- and Intermediate-Level Radioactive Waste in Sweden (SKB, 2008).

Plutonium is a highly relevant radionuclide in the context of nuclear waste disposal because of its high alpha radiotoxicity, redox characteristics and the long half-live of ^{239}Pu ($t_{½}$ $^{239}Pu = 2.41 \cdot 10^4$ a). In aqueous media, four oxidation states of plutonium can be thermodynamically stable, namely + III, +IV, +V and +VI. Among these, the predominance of Pu(III) and Pu(IV) is expected under repository relevant, reducing conditions (Neck et al., 2007). The chemical behavior of plutonium (e.g. solubility, complexation, sorption, etc.) is largely impacted by its redox state, which accordingly deserves dedicated experimental efforts under repository-relevant conditions. While the main stream of Pu will not be directed to L/ILW repositories, its presence cannot be totally excluded due to historical practices.

The radioactive waste disposed of in L/ILW repositories may contain cellulosic material (paper, textile, wood, etc.). Such materials are

* Corresponding author.
** Corresponding author.
E-mail addresses: agost.tasi@kit.edu (A. Tasi), xavier.gaona@kit.edu (X. Gaona).

chemically not stable in the hyperalkaline pH conditions imposed by cementitious environments, and will degrade into smaller chained organic substances generally named as cellulosic degradation products (CDPs). In Ca(II)-rich alkaline solutions, D-isosaccharinic acid was found to be the main degradation product of cellulose, representing up to 80% of the total degraded material (Bradbury and Van Loon, 1997; Glaus and Van Loon, 2008; Glaus et al., 1999; Pavasars et al., 2003). Van Loon et al. (1999) reported the formation of equal proportions of the α– and β–diastereomer forms of the ligand (α–HISA and β–HISA, respectively, for schematic structures see Figure SI-1 in Supporting Information). Several investigations have also observed the formation of relevant amounts of xyloisosaccharinic acid (XHISA, see Figure SI-1) in the alkaline degradation of hemicellulose, a component present in wood-related conglomerates (Aspinall et al., 1956; Gakhokidze, 1980).

The study of these polyhydroxocarboxylic acids is highly relevant in the context of nuclear waste disposal because of their strong complexing capabilities with actinides and other metal cations, especially under alkaline to hyperalkaline pH conditions where other organic ligands are hardly able to outcompete hydrolysis (Gaona et al., 2008; Hummel et al., 2005). In spite of its relevance, only a limited number of these studies were dedicated to Pu (see section SI-2.1.1 in Supporting Information).

Most of the studies investigating the interaction of radionuclides with CDP's have focussed on α-HISA, primarily because of the established synthetic paths for this diastereomer, but also because of the stronger complexation observed for some systems compared to β–HISA (Van Loon and Glaus, 1998). Note, however that a recent study investigating the complexation of HISA with Ni(II) reported a greater stability for the complex of Ni(II) with β–HISA than α–HISA (Almond et al., 2016). The same authors attributed a significantly weaker complexation capacity to XHISA, especially under hyperalkaline pH conditions where no Ni(II)–XHISA complexes were observed to be forming. The validity of the latter study was put in question by González-Siso et al. (2017), due to the largely oversaturation conditions with respect to β–$Ni(OH)_2$(s) used in the work of Almond et al. (2016).

In a comprehensive study by Randall et al. (2013), solubility experiments provided evidence of a strong complexation of XHISA with Th(IV) and Eu(III) under alkaline conditions. However, the authors concluded that due to the low concentration of XHISA in the various investigated leachates, the effect of CDPs on radionuclide behavior could be properly explained by assuming α–HISA as the dominant complexing ligand. In contrast to their solubility results, XHISA only showed a minor impact on the sorption of Th(IV) and Eu(III) onto the NIREX Reference Vault Backfill (NRVB) material, hematite and kaolinite.

Owing to its strong complexing properties and high abundance in CDPs, α–HISA is of great concern in performance assessment (PA) for radioactive waste disposals due to the potential implications in the mobilization of radionuclides. In a recent study, Keith-Roach et al. (2014) estimated the degree of cellulose degradation over time applying the kinetic model proposed by Glaus and Van Loon (2008). The original model, based on a 12-year-long degradation experiment of 4 different cellulosic materials under artificial cement porewater conditions, was extrapolated to (SFR 1) repository conditions and timescales (> 5000 years). The performed calculations show that the cellulose content of Tela tissue and paper will be completely degraded (~99%) after 5000 years, whereas longer times (~25000 years) will be needed for the complete degradation of cotton. Concentrations of ISA in the pore water were estimated using a conservative model for certain waste packages in SFR 1, with and without assuming the sorption of the ligand on cement. Upper limit calculations showed that, after 1000 years of cellulose degradation, the concentration of α–ISA reaches the solubility limit of Ca(α–ISA)$_2$(s) ($\approx 2{\cdot}10^{-2}$ M) in most of the waste packages during the stage of cement degradation controlled by portlandite. Including sorption processes in the evaluation of the free ligand concentration decreased this value to a maximum of $1.2{\cdot}10^{-2}$ M (including both α– and β–forms).

In this context, the objective of the current work is to evaluate the impact of α–ISA on the solubility of Pu under alkaline to hyperalkaline pH values and controlled redox conditions (hereafter the α–form of the ligand is denoted simply as HISA or as ISA, in its deprotonated state). The final goal is to provide experimentally based upper solubility limits for Pu in the investigated systems, and to derive complete and accurate chemical and thermodynamic models. The provided models can be then implemented in thermodynamic databases and thus further used in geochemical calculations of relevance for the Safety Case. Our previous comprehensive study on the solubility of Pu under analogous pH and redox conditions (but in the absence of ISA) is taken as the 'reference baseline' for the interpretation of Pu solubility behavior, against which the impact of ISA on the solution chemistry of plutonium can be accurately quantified under the investigated boundary conditions (Tasi et al., 2018).

2. Complexation of ISA with An(III)/Ln(III) and An(IV)

The complexation of ISA with An(III)/Ln(III) and An(IV) was previously investigated in a number of solubility (Colàs, 2014; Greenfield et al., 1995, 1997; Kobayashi et al., 2017a; Moreton, 1993; Moreton et al., 2000; Rai et al., 1998, 2003, 2004, 2009; Randall et al., 2013; Warwick et al., 2004), sorption (Greenfield et al., 1997; Vercammen, 2000; Vercammen et al., 1999, 2001), spectroscopic (Colàs, 2014; Zhang et al., 2009) and solvent extraction studies (Allard et al., 2008). These studies reported the formation under near-neutral to hyperalkaline pH conditions of binary and ternary complexes with general formulae: $M(III/IV)(ISA)_y^{(+3/+4-y)}$ and $M(III/IV)(OH)_x(ISA)_y^{(+3/+4-x-y)}$, respectively. A detailed overview on the experimental studies available in the literature is provided in the Supporting Information (see section SI-2.). For all these systems, the Nuclear Energy Agency - Thermochemical Database (NEA-TDB) review (Hummel et al., 2005) on the complexes of U, Np, Pu, Am, Tc, Se, Ni and Zr with selected organic ligands is taken as the most authoritative reference. Two review works (Gaona et al., 2008; Rai and Kitamura, 2017) dedicated to the complexation of ISA with radionuclides and other elements relevant in the context of nuclear waste disposal were published since the release of the NEA-TDB book. These publications did not provide new experimental results, but focus on the critical review of the available thermodynamic studies.

One of the open questions affecting the complexation of ISA with actinides (and with metal cations in general) is the possible role of the aliphatic hydroxyl functional groups (often denoted as alcohol groups) of ISA on the chelation of the metal cation. Although the pK_a of the α–OH group of ISA was estimated (Evans, 2003) as ≈ 14.3, the enhanced acidity of this hydroxyl group caused by the complexation with a metal cation is expected to result in the deprotonation of the α– (and even γ–) hydroxyl functional group under significantly less alkaline conditions. Hence, the protons released in the complex formation under alkaline conditions can be assigned to both processes: (i) hydrolysis of the metal cation and (ii) deprotonation of alcohol groups:

$$M^{n+} + x\,H_2O(l) + ISA^- \Leftrightarrow M(OH)_xISA^{n-x} + x\,H^+ \quad (1)$$

$$M^{n+} + y\,H_2O(l) + ISA^- \Leftrightarrow M(OH)_y(ISA_{-zH})^{n-z-y} + (y+z)\,H^+ \quad (2)$$

where $x = (y + z)$ and $ISA_{-zH}^{-(1+z)}$ corresponds to an ISA ligand with the deprotonated carboxylic and z number of alcohol groups. The choice of one or the other complexation mode has no implications in the mass-action laws and, therefore, it does not affect the calculated equilibrium constants. For the sake of consistency with most of the previous studies, the first option (hydrolysis of the metal cation) is adopted initially in the following sections to generally describe chemical formulae of An/Ln–ISA complexes. An in-depth discussion of the different complexation modes of ISA with plutonium is provided in section 4.3.1 based upon density functional theory (DFT) calculations

performed in this study.

The spectroscopic analysis of the coordination mode in An–ISA complexes is frequently hindered by the sparingly soluble solid phases controlling the solubility of actinides in alkaline conditions, and the low actinide concentration in solution. The higher solubility of Th(IV) compared to other An(IV) was used by Colàs (2014) to investigate the structure of Th(IV)–ISA and Th(IV)–GLU complexes using EXAFS. Although the results were not conclusive, spectroscopic data suggested that one or more alcohol groups participate in the complexation with Th(IV). As for the U(VI)-GLU system under acidic conditions, Zhang and co-workers were able to identify deprotonated hydroxyl functional groups (alcoholate) being coordinated to the metal centre combining results of pH-potentiometric and calorimetric titrations in combination with NMR and EXAFS investigations (Zhang et al., 2009). In their comprehensive work, the authors presented the first unequivocal experimental evidence for the coordination-induced deprotonation of the alcohol group during the complex formation reaction. The use of DFT calculations were also shown to provide relevant insights in the study of the structure of actinide complexes with organic ligands. In a combined solubility, ^{13}C NMR and DFT study, Felmy and co-workers investigated the aqueous complexation of thorium with citrate under neutral to basic conditions (Felmy et al., 2006). For this system, quantum chemical calculations suggested that the α-hydroxyl proton of citrate can be displaced during complex formation with Th(IV). The U(VI)–ISA system was studied by Birjkumar et al. (2012) using ground state and time-dependent DFT calculations. The authors evaluated the impact of pH by varying the number of water and hydroxide ligands in the equatorial plane of the uranyl moiety[1]. At "high pH", Birjkumar and co-workers observed that the most favoured geometry was obtained for a 6-membered chelate ring involving the carboxylic group and the -OH group in C6 (see Figure SI-1). However, the energetic differences with other coordination modes (involving 5- and 4-membered chelates) were not sufficient to rule out the possibility that multiple species coexist. So far, no such theoretical calculations are available for An(III) and An(IV) complexes with ISA.

3. Experimental section

All experiments with plutonium were performed in specialized α-laboratories in the controlled area of KIT–INE. All experiments were conducted in Ar gloveboxes with O_2 concentration below 10 ppm and under carbonate exclusion.

3.1. Chemicals

All solutions were prepared with ultra–pure water purified with a Milli–Q apparatus (Millipore, 18.2 MΩ, 22 ± 2 °C) and purged for several hours with Ar before use. Milli–Q water used for the preparation of solubility samples in the presence of ISA was further boiled for several hours and simultaneously purged with Ar. $C_8H_{17}NO_3S$ (CHES; p.a.), NaCl (p.a.), NaOH (Tritrisol), HCl (Tritrisol), $Na_2S_2O_4$ (> 87%), hydroquinone (p.a.), xylene (isomeric mixture, p.a.) and toluene (p.a.) were obtained from Merck. $C_4H_{11}NO_3$–$C_4H_{11}NO_3$·HCl (TRIS–TRIS·HCl; p.a.) and $SnCl_2$ (p.a.) were purchased from Sigma–Aldrich. 1-phenyl-3-methyl-4-benzoyl-pyrazol-5-one (PMBP) and Di-(2-ethylhexyl)-phosphoric acid (HDEHP) were obtained from Fluka (purum). Carbonate impurities in fresh 1.00 M NaOH (Titrisol) were quantified as $(3 \pm 1)\cdot10^{-5}$ M using a Shimadzu TOC5000 equipment. $Ca(ISA)_2(s)$ [$CaC_{12}H_{22}O_{12}$] was purchased from Alfa Aesar. Although the purity of $Ca(ISA)_2(s)$ indicated by Alfa Aesar was > 98% (Assay), the characterization of this material revealed a significant content of carbonate which was removed in a purification step after the synthesis of NaISA(s). The synthesis of NaISA(s) from commercial $Ca(ISA)_2(s)$ involved the use of an ion exchange resin (Chelex® 100, Na-form, Sigma Aldrich, analytical grade purity) and diethyl-ether ($C_4H_{10}O$, ACS reagent grade, VWR BDH Prolabo®). A detailed description of the synthesis, purification and characterization of NaISA(s) is provided in section SI-3, within Supporting Information. The resulting NaISA stock solution was characterized as (0.16 ± 0.02) M NaISA with pH_m = 8.9. The stock solution contained also an excess of sodium in the form of chloride, thus resulting in 0.16 M NaISA, plus 0.18 M NaCl.

The isotopic composition of Pu stock solution and solid phases used in this study was 99.4 wt % ^{242}Pu, 0.58 wt % ^{239}Pu, 0.005 wt % ^{238}Pu and 0.005 wt % ^{241}Pu. The use of the long-lived ^{242}Pu isotope ($t_{½}$ = 3.75·10^5 a) avoids redox processes induced by radiolysis.

3.2. Measurements of pH and E_h

Combination pH–electrodes (type Orion Ross, Thermo Scientific), freshly calibrated against standard pH buffers (pH = 8–13, Merck) were used to determine the total free concentration of proton in molar (pH_c = –log [H^+]) or molal units (pH_m = –log m_{H^+}). In aqueous solutions of ionic strength $I_m \geq 0.1$ mol kg^{-1}, the measured pH value (pH_{exp}) is an operational apparent value related to m_{H+} ([H^+]) by $pH_m = pH_{exp} + A_m$ ($pH_c = pH_{exp} + A_c$), where A_m (A_c) is an empirical parameter including the activity coefficient of the proton (γ_{H^+}) and the liquid junction potential of the electrode for a given background electrolyte and ionic strength (and temperature, pressure). The empirical A_m (A_c) values for NaCl were taken from the literature (Altmaier et al., 2003). In NaCl–NaOH solutions with $m_{OH^-} > 0.03$ m, the H^+ concentration was calculated from the given m_{OH^-} and the conditional ion product of water (K'_w) at the ionic medium concentration used in the experiments. The latter was calculated from the standard state constant (K°_w) extrapolated by the Specific Ion interaction Theory (SIT) approach using the parameters from the NEA-TDB compilations (Guillaumont et al., 2003).

The redox potential was determined with combined Pt or Au and Ag/AgCl reference electrodes (Metrohm). The measured potentials were converted to E_h (*versus* standard hydrogen electrode: SHE) by correcting for the potential of the Ag/AgCl inner-reference electrode with 3 M KCl and T = 22 °C (+207 mV). E_h values were converted to pe = –log a_{e^-} according to equation (3):

$$E_h = -RT \ln(10)\, F^{-1} \log a_{e^-}, \quad (3)$$

where R is the ideal gas constant (8.31446 J mol^{-1} K^{-1}), F is the Faraday constant (96485.33 C mol^{-1}) and a_{e^-} is the activity of the electron. E_h values of the solutions were collected following the protocol described by Altmaier et al. (2010), which involved approximately 15 min of equilibration time. Sufficiently stable E_h readings were obtained in hydroquinone– (HQ) and in many of the Sn(II)−-containing samples, when the absolute drift of the electrode was observed to be < 0.5 mV/min after the indicated time. The uncertainty of E_h values collected within 15 min of equilibration time ranged between ± 15 and ± 30 mV (calculated as 2σ of repeated E_h readings). E_h measurements in Sn(II)-buffered systems with pH_m < 11 normally required longer equilibration times. This is mostly due to the sparingly soluble Sn(II)-oxides and -oxy-hydroxides forming in these conditions (Gamsjäger et al., 2012): SnO(cr), or ($Sn_6O_8H_4$(s)/$Sn_6O_4(OH)_4$(s)), and the accordingly low reducing $[Sn(II)]_{tot}$ in solution. For these critical samples, E_h values were collected repeatedly with increasing equilibration times (15 min, 1, 2 and 6 h). Longer equilibration times resulted in significantly lower absolute drift of the redox potential (< 0.08 mV min^{-1}), leading also to clearly lower numerical deviations

[1] The authors performed calculations at "low pH", "neutral pH" and "high pH", involving the reaction of UO_2^{2+}, $UO_2(OH)_2$(aq) and $UO_2(OH)_4^{2-}$, respectively with ISA. Calculations at "very high pH" were analogous as those at "high pH", but involved the deprotonation of the α-OH group of ISA in the process of complex formation. No specific pH values were assigned to the different pH regions investigated.

in the measured values (± 10 to ± 16 mV, calculated as 2σ of repeated E_h readings, see Table SI-2 in Supporting Information). This was considered to be a satisfactory compromise between the accuracy of the E_h readings and the length of the solubility experiments.

3.3. Pu-ISA solubility experiments

The system Pu–ISA was investigated in four experimental series with a total of 34 independent batch samples. Redox conditions were set by using 2 mM of either HQ (with pe + pH_m ~ 9) or Sn(II) (with pe + pH_m ~ 1.5). In the presence of each redox buffering agent, two series of solubility experiment were prepared:

a. pH_m varied from 8 to 12.9, and $[ISA]_{tot}$ = constant = 10^{-3} M. For the HQ system, an additional series at $[ISA]_{tot}$ = 0.01 M was prepared.
b. pH_m = constant = 12, and $[ISA]_{tot}$ varied from 10^{-6} to 0.10 M.

Solutions at pH_m = 8 and 9 were pH buffered with 20 mM of TRIS and CHES, respectively. The ionic strength of the solutions was kept constant at 0.10 M NaCl–NaOH–NaISA, except for the sample with the highest ISA concentration (0.10 M), where the individual ionic strength of the NaISA stock solution set the overall ionic strength to a higher value, I = 0.23 M. Before the addition of the Pu solid phase, the pH_m values of the matrix solutions were adjusted with HCl and NaOH solutions of same ionic strength. After achieving constant readings of pH_m and E_h, approximately 0.25 mg of a nanocrystalline Pu(IV)O_2(ncr,hyd) solid phase (aged in 0.10 M NaCl solution for *ca.* 8 years) were added to each individual batch sample. A larger amount (1.5–2.5 mg) was added to six samples with pH_m = 9 and 12 ($[ISA]_{tot}$ = 10^{-3} M) and with $[ISA]_{tot}$ = 0.10 M (pH_m = 12) (for both, HQ- and Sn(II)-buffered systems), intended to allow for a later comprehensive solid phase characterization. The structural properties and solubility behavior of the initial material are published elsewhere (Tasi et al., 2018). After the addition of the solid phase, pH_m, E_h and $[Pu]_{tot}$ were regularly monitored for 90 days. Equilibrium conditions (constant pH_m, E_h and $[Pu]_{tot}$ values) were normally attained within 30 days of contact time.

3.4. Characterization of the aqueous phase

The aqueous total concentration of Pu was quantified by liquid scintillation counting (LSC), Quadrupole ICP–MS or sector field inductively coupled plasma mass spectrometry (SF–ICP–MS, PerkinElmer, Elan 6100). Phase separation was achieved by ultrafiltration with 10 kD filters (pore size ≈ 2 – 3 nm, Nanosep®, Pall Life Sciences) or, for selected samples, by ultracentrifugation (Beckman XL-90, rotor type 90Ti) at 90000 rpm (694000 g) for 1 h. Concentration of Pu in the supernatant without any phase separation was also measured by LSC or ICP–MS to evaluate the possible presence of Pu(IV) (intrinsic) colloids or other colloidal species to which Pu could be associated. In the case of analysis with ICP–MS, and SF–ICP–MS, an aliquot of the sample was immediately acidified with 2% HNO_3 with appropriate dilution factors. The detection limits (DL) of these techniques for Pu in the conditions of this study are ~$10^{-10.5}$ M and ~10^{-13} M, respectively. For LSC, the concentration of Pu in solution was quantified using the signal of the low-energetic β-emitter ^{241}Pu. The detection limit of LSC for Pu in the conditions of this study is ~$10^{-9.2}$ M. Aliquots of the solution after or before phase separation (clear supernatant) were acidified with 2% HNO_3 and further mixed with 10 mL of LSC cocktail (Ultima Gold XR, Perkin Elmer). LSC measurements were performed on a low-level LSC equipment type Quantulus 1220 (LKB WallacOy, Turku, Finland, PerkinElmer) for 30 min. Standard addition with 50 µL of a well-defined Pu stock solution ($4.36 \cdot 10^{-7}$ M or $3.18 \cdot 10^{-7}$ M) with the same isotopic composition was used to overcome the effect of the matrix solution on the counting efficiency of ^{241}Pu of unknown samples. Detection limits of the above mentioned analytic techniques were determined as three times the mean standard deviation (3σ) of the measurement of blank samples, and considering the dilution step/s involved in the measurement of unknown samples.

The detected plutonium concentrations in molar units (M) (and all other concentrations evaluated in this study) were converted to the molal scale (m, mol·kg_w^{-1}) using the conversion factors reported for NaCl solutions in the NEA-TDB (Guillaumont et al., 2003).

3.5. Characterization of the solid phase

XAFS (X-ray Absorption Fine Structure) spectra and Laue-type *in-situ* diffractograms of selected solid phases were recorded at the INE–Beamline for Actinide Research at ANKA, KIT Campus Nord (Rothe et al., 2012). The ANKA storage ring was operated at 2.5 GeV electron energy with a mean electron current of 120 mA.

The tuneable monochromatic beam was delivered by a double crystal monochromator (DCM), equipped with a pair of Ge(422) crystals (2d = 2.310 Å). Possible higher harmonic radiation was suppressed by detuning the parallel alignment of the crystals to obtain 70% of photon flux peak intensity at the rocking curve maximum.

All samples for XAFS and *in-situ* XRD measurements were prepared in 400 µL polyethylene vials and strictly kept under protective atmosphere. A suspension containing ≈1 mg of material was transferred to the vial and centrifuged for 10 min at 4020 g. The vial was heat sealed in a plastic bag (polyethylene), mounted in a gas-tight cell inside the Ar-glovebox and transported to the INE-Beamline. During the XAFS measurements, Ar was continuously flushed through the cell to ensure inert atmosphere. Data collection was performed at T = (22 ± 2) °C.

XANES spectra of the Pu L_{III}-edge (E ($2p_{3/2}$) Pu^0: 18057 eV) were recorded in fluorescence yield detection mode using a 5-pixel low energy Ge solid-state fluorescence detector (Canberra-Packard Ultra-LEGe, Olen, Belgium) and an Ar-filled ionization chamber at ambient pressure to record the incident beam intensity. 8 – 10 scans were collected for each Pu sample. The spectra were calibrated against the first inflection point in the K-edge spectrum of a Zr metal foil (E (1s) Zr(0): 17998 eV) and averaged to reduce statistical noise. XANES and EXAFS data reduction were performed with the ATHENA program package (Ravel and Newville, 2005), following standard procedures for edge jump normalization and EXAFS χ(k) extraction. E_0, the origin for calculating the EXAFS χ(k)-function, was fixed at the 'white line' (WL) peak maximum in the XAFS spectra at ≈ 18068 eV. The Pu L_{III}-edge XANES spectra obtained in this work were compared with Pu(III) and Pu(IV) reference spectra collected at the INE-Beamline under the same experimental conditions and data analysis procedure (Brendebach et al., 2009; Walther et al., 2009).

EXAFS data analysis was based on standard least squares fit techniques using the UWXAFS program package (Stern et al., 1995). Metric parameters (i.e., neighbour atom distances R_i, EXAFS Debye-Waller factors σ_i^2, coordination numbers N_i for the different coordination shells i) were determined using the FEFFIT code (v2.98). Backscattering amplitude and phase shift functions for single scattering paths in a 45-atom PuO_2 cluster with fluorite structure were obtained from FEFF8.2 calculations (Ankudinov et al., 1998). All fit operations were performed in R-space over the individual radial distance ranges as described in section 4.1.3.3. The amplitude reduction factor S_0^2 was fixed at 1.0.

After completing the XAFS data accumulations, the samples were individually taken out of the Ar-flushed sample cell, and the *in-situ* diffractograms were collected. The double containment (vial and an outer plastic bag) in addition to the redox buffers in the protecting solution (hydroquinone and Sn(II)) underneath the Ar atmosphere are considered to be sufficient to avoid any redox transformation of the bulk material within the short timeframe of the XRD measurements (approximately 5–10 min).

The 2D XRD patterns were recorded in Laue transmission geometry using radiation sensitive high efficiency storage phosphor screens (V × H: 125 mm × 252 mm) with a high dynamic range

(MultiSensitive Phosphor Screen, PerkinElmer, Germany). The screen was mounted perpendicular to the incident beam (E = 17.0 keV, λ_{exc} = 0.7 Å, size (V × H) 200 µm × 500 µm) at a distance of 20 cm from the sample. An indium metal disk, mounted on the tip of a plastic rod was used as central beam-stop. The irradiated phosphor screen was scanned by a laser based read-out system (Cyclone Plus Phosphor Imager, PerkinElmer LAS, Rodgau-Jügesheim, Germany), transforming the diffracted 2D X-ray intensity into a high resolution digitized image (600 dpi) with quantitative data as an image file (OptiQuant™ software).

The collected frames were transformed into one-dimensional diffraction patterns by using the XRDUA software package (De Nolf et al., 2014). The images were corrected for dark-current, spatial distortion and detector pixel response. The XRD pattern of an Y_2O_3 powder sample was used as reference for calibration (Smrcok, 1989). After correcting and calibrating the images, azimuthal integration was performed and the resulting diffractograms were normalized for the incident beam intensity. The background subtraction was achieved with a cubic spline polynomial fitting of the baseline.

The specific set-up available at the INE–Beamline for the *in-situ* XRD characterization of active samples is a unique, non-invasive tool for the investigation of redox-sensitive solid phases and contributed significantly to the success of this study.

3.6. Data evaluation and modelling methods for deriving thermodynamic quantities

After deriving the corresponding chemical models, experimental solubility data sets were evaluated with the final aim of obtaining the thermodynamic models describing the investigated Pu–ISA system. Two different approaches were used to derive these thermodynamic quantities: the Solver tool of Microsoft Excel and the PHREEPLOT-PHREEQC (PP–PQC) program packages (version 3.3.5, svn 10806) (Kinniburgh and Cooper, 2009; Parkhurst and Appelo, 1999, 2013). The Specific Ion-interaction Theory (Ciavatta, 1980) (SIT) was used for ionic strength corrections. Ion-interaction parameters ($\varepsilon_{i,j}$) of the newly formed complex species were estimated based on the charge correlation approach described by Hummel (2009). Note that due to the relatively low ionic strength in all the experiments (I = 0.10 m), the main contribution to the activity corrections results from the Debye–Hückel term rather than the ion-interaction parameters. Hence, the use of estimated $\varepsilon_{i,j}$ values taken from analogy has a limited impact on the calculated values of the equilibrium constants at I = 0. Although simultaneously a maximum of two parameters were optimized, the reproducibility of the resulting values was further tested by the systematic variation of the initial input estimates. To gain further confidence on the obtained numerical results, the corresponding objective functions were minimized by the use of both, gradient-based (modified Levenberg-Marquardt method, (Powell, 1965)) and non-gradient-based (SIMPLEX method, (Nelder and Mead, 1965)) methods.

3.7. Theoretical methods

The structures of the Pu(IV)–OH–ISA and Pu(III)–OH–ISA complexes were investigated with density functional theory (DFT) calculations (Hohenberg and Kohn, 1964; Kohn and Sham, 1965). DFT calculations were performed using TURBOMOLE (version 7.0, 2015) (Ahlrichs et al., 2015; Deglmann et al., 2004; Eichkorn et al., 1995; Eichkorn et al., 1997; Schäfer et al., 1992; Treutler and Ahlrichs, 1995; von Arnim and Ahlrichs, 1999) with the BP86 functional (Ahlrichs et al., 2000) and the def2-SVP basis set (Schäfer et al., 1992) on C, O and H. The use of 5f-in core pseudo potentials (PP) for Pu(III) (Moritz et al., 2006) and Pu(IV) (Moritz et al., 2007) allowed to circumvent several problems arising with DFT calculations involving actinides: (i) difficulties due to open shells can be avoided, (ii) multi reference effects do not occur and (iii) the number of electrons and thus the computer time is greatly reduced. This leads to a theoretical task suited for DFT, and avoids complex and computational very demanding multi reference ab initio methods.

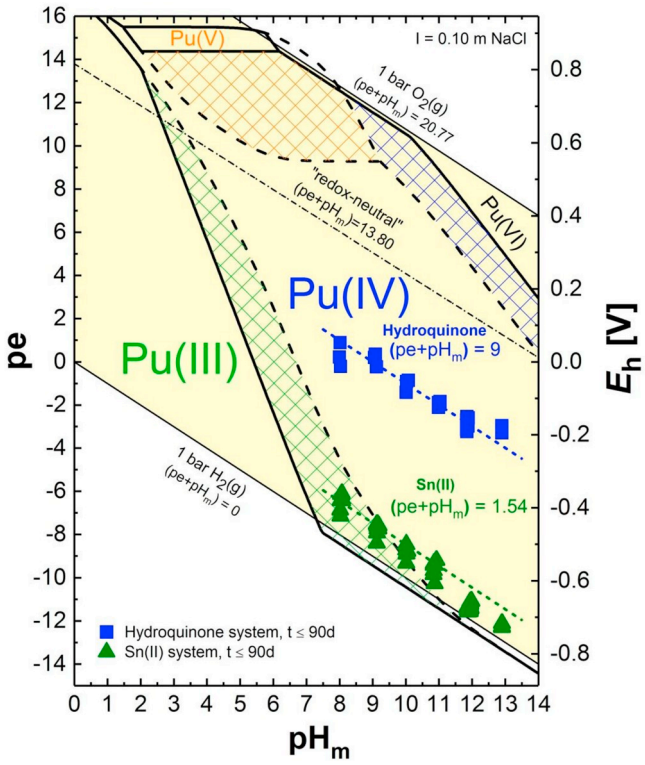

Fig. 1. Pourbaix diagram of Pu calculated for $m_{Pu} = 10^{-5}$ m and I = 0.1 m NaCl using the thermodynamic data and (SIT) parameters as described in the text. pH_m and E_h values experimentally determined for Pu(IV) solubility experiments in the presence of ISA and redox-buffering agents: hydroquinone (■) and Sn(II) (■). Bold lines correspond to redox borderlines between Pu(IV) and other Pu redox states with the solid line reflecting the borderline between Pu solid phases. Dashed line is the redox borderline between Pu aqueous species. Colored regions indicate equilibrium between $Pu(IV)_s$ and $Pu(III)_{aq}$ (green), $Pu(V)_{aq}$ (orange) and $Pu(VI)_{aq}$ (blue). The borderlines of the stability field of water at (pe + pH_m) = 20.77 and (pe + pH_m) = 0, the "redox-neutral" line at (pe + pH_m) = 13.8 and the lines at (pe + pH_m) = 1.54 and 9 are shown for comparison. (For interpretation of the references to colour in this figure legend, the reader is referred to the Web version of this article.)

For a more realistic description of the Pu(III/IV)–OH–ISA systems investigated, several water molecules saturating the alcohol groups of the ISA and the Pu ion were considered in the calculations. A second step in the calculations included the aqueous media approximated with the conductor-like screening model (COSMO) (Klamt, 1995; Klamt and Schuurmann, 1997). Considering the first water shell explicitly and dealing with the additional solvation effects by means of COSMO provides a realistic model to investigate species in aqueous solution.

4. Results and discussion

4.1. Pu-ISA experiments

4.1.1. pH and E_h measurements

The experimentally measured pH_m and E_h (converted into pe) values of all the evaluated samples are shown in the Pourbaix diagram of Pu in Fig. 1. Thermodynamic solubility and hydrolysis constants for plutonium reported in Neck et al. (2007) were used for the calculations. SIT ion interaction parameters estimated in the work of Neck and Kim (2001) were used to account for ionic strength corrections of Pu(IV), whereas ε(i,j) values reported in Neck et al. (2009) for Am(III) and Nd

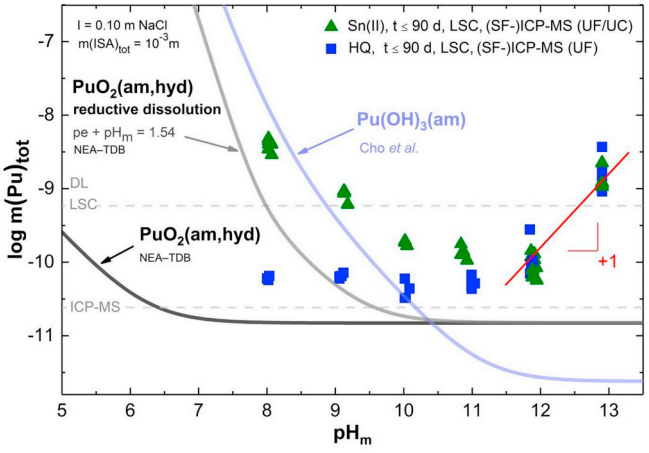

Fig. 2. Experimentally measured $m(Pu)_{tot}$ in equilibrium with PuO_2(ncr,hyd) in 0.10 m NaCl for redox buffered systems with HQ (■) and Sn(II) (■) at pH_m = 8 – 12.9 and $m(ISA)_{tot} = 10^{-3}$ m. Solid lines correspond to the thermodynamically calculated solubility of PuO_2(am,hyd) in the absence of ISA: black line (in equilibrium with $Pu(IV)_{aq}$ species only), and for (pe + pH_m) = 1.54: grey line, predominance of $Pu(III)_{aq}$ below $pH_m \approx 10.5$ (see text for more details) calculated according to NEA-TDB (Guillaumont et al., 2003). The light blue line designates the solubility curve of $Pu(OH)_3$(am) in equilibrium with $Pu(III)_{aq}$ species calculated by using log $^*K^\circ_{s,0}$ reported in Cho et al. (2016). Red line with a slope of +1 is shown for comparison purposes. UF and UC indicate the use of ultrafiltration and ultracentrifugation as phase separation methods. (For interpretation of the references to colour in this figure legend, the reader is referred to the Web version of this article.)

(III) were taken for the corrections of Pu(III) aqueous species. ε(i,j) values reported in Gaona et al. (2013) for Np(VI) were taken for the SIT corrections of the analogous Pu species.

Solubility experiments with HQ or Sn(II) redox buffered systems in the presence of ISA showed stable pH_m (± 0.05) and E_h (± 10–30 mV, depending upon pH_m-region) readings within the time frame of this study (90 days).

In accordance with the findings of our previous Pu study conducted under very similar conditions but in the absence of ISA (Tasi et al., 2018), the use of HQ as a redox buffering agent set moderately reducing conditions with (pe + pH_m) = (9 ± 1). These conditions fall within the stability field of $Pu(IV)_s$ and $Pu(IV)_{aq}$, and thus this system is considered as the reference case to assess the interaction of $Pu(IV)_{aq,s}$ with ISA. On the other hand, the presence of Sn(II) maintained strongly reducing conditions in solution. Redox potentials observed in all Sn(II)-buffered systems with shorter measurement time (approximately 15 min, for samples with $pH_m \geq 11$) are well-described by (pe + pH_m) = (1 ± 1). As discussed in section 3.2, longer measuring times were required for Sn(II) samples with $pH_m < 11$. For these systems, the use of E_h measurements after 1, 2 and 6 h resulted in (pe + pH_m) = (1.54 ± 0.14) (with uncertainty calculated as 2σ). Note that the reductive dissolution of PuO_2(am, hyd) ⇔ Pu(III)–ISA (aq) is proposed to control the solubility of Pu in Sn(II) systems with $pH_m < 11$ (see section 4.2.2), and thus uncertainties in pe are directly transferred to log K° values determined from solubility data.

4.1.2. Solubility measurements

The total concentrations of plutonium in equilibrium with PuO_2(ncr,hyd) and in the presence of NaISA measured after phase separation (ultrafiltration or ultracentrifugation) are shown in Fig. 2 (pH_m = 8 – 12.9; $m(ISA)_{tot}$ = constant = 10^{-3} m) and Fig. 3 (a,

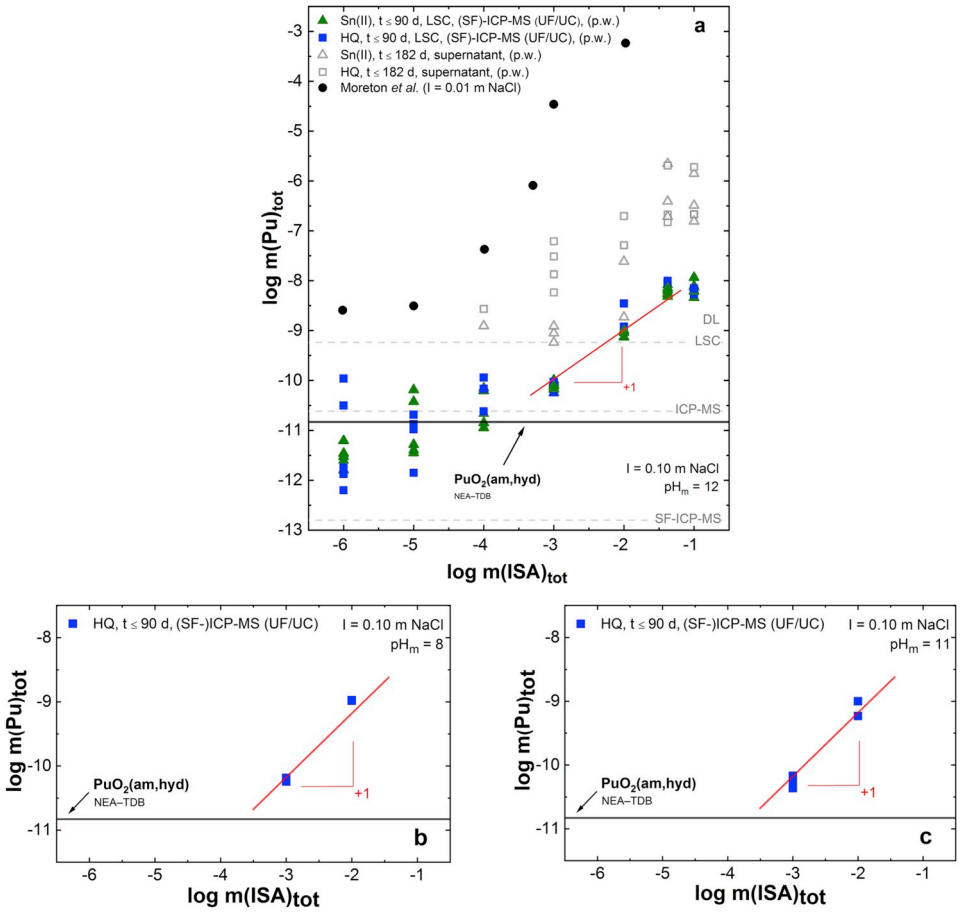

Fig. 3. Experimentally measured $m(Pu)_{tot}$ in equilibrium with PuO_2(ncr,hyd) in 0.10 m NaCl for redox buffered systems with HQ (■) and Sn (II) (■) at pH_m = 12 (**a**), pH_m = 8 (**b**) and 11 (**c**) and 10^{-6} m ≤ $m(ISA)_{tot}$ ≤ 0.10 m. Open symbols are the total concentrations of Pu in the supernatants of the Sn(II)– (Δ) and HQ–buffered (□) systems (no phase separation). Black circles (●) correspond to experimental solubility data reported in Moreton et al. (2000) obtained from oversaturation conditions at I = 0.01 m NaCl. Solid black line corresponds to the solubility of PuO_2(am,hyd) in equilibrium with $Pu(IV)_{aq}$ and in the absence of ISA, calculated according to NEA-TDB thermodynamic selection (Guillaumont et al., 2003). Red lines with m $(Pu)_{tot}$ *vs.* $m(ISA)_{tot}$ slopes of +1 are shown for comparison. (For interpretation of the references to colour in this figure legend, the reader is referred to the Web version of this article.)

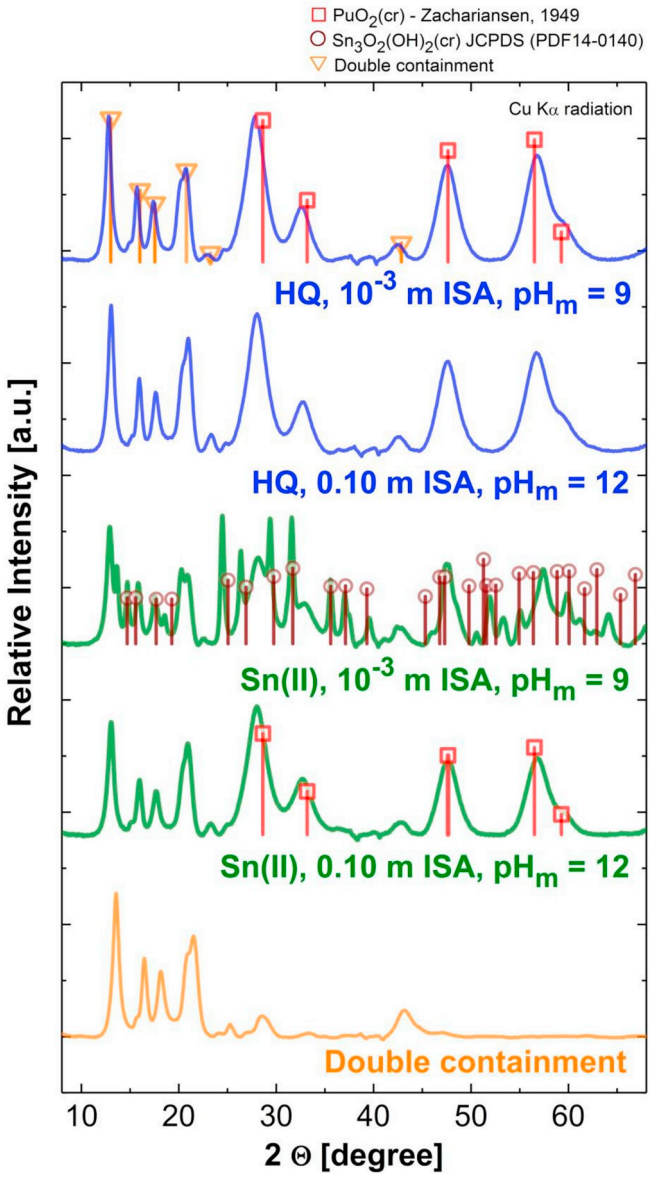

Fig. 4. Background corrected, normalized *in-situ* XRD patterns acquired at INE-Beamline for the Pu solid phases recovered (t_{eq} = 260 days) from HQ-buffered (blue lines) and Sn(II)-buffered (green lines) solubility experiments with m $(ISA)_{tot} = 10^{-3}$ m at $pH_m = 9$ and $m(ISA)_{tot} = 0.10$ m at $pH_m = 12$, and also for the empty double containment (orange line and triangle symbols). Square and circle marks show peak positions and relative intensities reported in Zachariansen (1949) for PuO_2(cr) and for $Sn_6O_4(OH)_4$(cr) (PDF 14–0140) adapted from JCPDS database (Wong-Ng et al., 2001), respectively. (For interpretation of the references to colour in this figure legend, the reader is referred to the Web version of this article.)

pH_m = constant = 12; $m(ISA)_{tot} = 10^{-6}$ – 0.10 m; b, pH_m = constant = 8; $m(ISA)_{tot} = 10^{-3}$, 0.01 m; c, pH_m = constant = 11; $m(ISA)_{tot} = 10^{-3}$, 0.01 m). Fig. 3 a also includes the total Pu concentrations measured in the supernatants of the solubility experiments (without phase separation applied). The latter data give insight on the possible presence of colloidal Pu(IV) species. The calculated solubility of PuO_2(ncr,hyd) in the absence of ISA in equilibrium with $Pu(IV)_{aq}$ (HQ system) and for (pe + pH_m) = 1.54 (reductive dissolution), as well as the solubility of $Pu(OH)_3$(am) using log $^*K^\circ_{s,0}$ reported in Cho et al. (2016) are appended to the figures for comparison.

4.1.2.1. Solubility of Pu at constant $m(ISA)_{tot}$ and increasing pH_m. Fig. 2 shows that very stable values of $m(Pu)_{tot}$ are obtained for both HQ and Sn(II) buffered systems after 90 days, indicating that thermodynamic equilibrium was attained within this timeframe. The trends observed in the solubility curves in HQ and Sn(II) systems can be divided in three different cases:

I. pH_m = 8 – 11 in HQ-buffered systems: moderate and pH_m-independent enhancement in the solubility of PuO_2(ncr,hyd), indicating that no H^+ are involved in the equilibrium reaction controlling the solubility of Pu. The increase in solubility with respect to the ISA-free systems is attributed to the formation of Pu(IV)–ISA aqueous complexes.
II. pH_m = 8 – 11 in Sn(II) systems: greater impact of ISA on the solubility of PuO_2(ncr,hyd), compared to the HQ system. The solubility shows also a clear pH-dependency with a slope (log $m(Pu)_{tot}$ *vs.* pH_m) close to −1. Such difference in behavior relative to the HQ case (I.) is attributed to the formation of Pu(III)–ISA aqueous complexes.
III. pH_m > 11 for both HQ and Sn(II) systems: clear increase in the Pu solubility with a slope (log $m(Pu)_{tot}$ *vs.* pH_m) ≈ +1, indicating that one H^+ is released in the equilibrium reaction controlling the solubility of Pu. The very similar behavior observed in HQ and Sn(II) suggests that Pu(IV)–ISA complexes prevail in both systems at this high pH.

4.1.2.2. Solubility of Pu at constant pH_m and increasing $m(ISA)_{tot}$. Fig. 3 shows the solubility of Pu at pH_m = constant = 12 (a), 8 (b) and 11 (c) under increasing $m(ISA)_{tot}$. At pH_m = 12 (Fig. 3 a), virtually the same solubility behavior is observed for HQ and Sn(II) systems, indicating that the same chemical equilibria is likely to control the solubility in both systems. Consistent values are obtained using ultrafiltration or ultracentrifugation as phase separation. A large scattering in $m(Pu)_{tot}$ is observed at $m(ISA)_{tot} < 10^{-3}$ m, in line with the results obtained in our previous work in the absence of ISA (Tasi et al., 2018). More precise quantifications of $m(Pu)_{tot}$ are obtained at $m(ISA)_{tot} \geq 10^{-3}$ m, indicating the formation of a new Pu(IV)–ISA complex. Note that the increased precision of solubility measurements (or better phase separation) upon formation of charged aqueous complexes was previously reported for the Th(IV)–carbonate system (Altmaier et al., 2005). At $m(ISA)_{tot} \geq 10^{-3}$ m, the solubility of Pu increases with a well-defined $m(Pu)_{tot}$ *vs.* $m(ISA)_{tot}$ slope of +1, indicating that the Pu:ISA stoichiometry of the complex at pH_m = 12 is 1:1.

The quantitative analysis of Pu in the supernatant solutions without any phase separation (open symbols in Fig. 3 a) show a significantly greater $m(Pu)_{tot}$ than the values obtained after ultracentrifugation or ultrafiltration, displaying that a large fraction of colloidal Pu(IV) aqueous species are stabilized in the presence of ISA. Special care was taken to avoid artefacts caused by the re-suspension of solid particles. The reproducibility of these observations was counterchecked with independent samples prepared with different total volumes and types of containers. Although $m(Pu)_{tot}$ values obtained after phase separation are representative of the thermodynamic equilibrium between the solid phase and monomeric aqueous species, the colloidal fraction must be also considered when assessing the impact of ISA on the mobilization of Pu under repository-relevant conditions and thus cannot be neglected.

Solubility data of Pu(IV) in the presence of ISA previously determined by Moreton et al. (2000) are also shown in Fig. 3 a. Substantial discrepancies exist between these data and the Pu solubility determined in the present work in both, HQ- and Sn(II)-buffered systems. Significant shortcomings were identified in the experimental set-up of Moreton and co-workers (see section SI-2.1.1.), most importantly the use of oversaturation approach without phase separation for the quantification of $m(Pu)_{tot}$ and non-redox buffered conditions, among others. Indeed, the $m(Pu)_{tot}$ concentrations measured in the present work in the absence of phase separation already point out that the

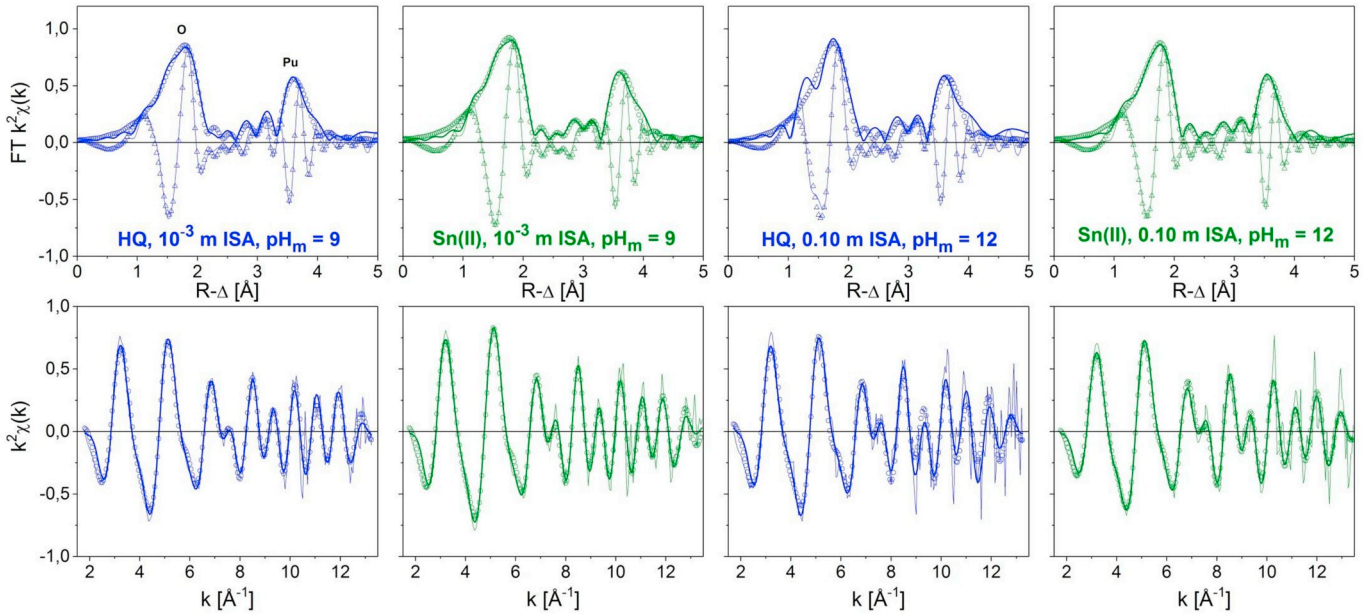

Fig. 5. Pu L_{III}–edge EXAFS fit results for Pu(IV)O_2(ncr,hyd) solid phases recovered from HQ and Sn(II)-buffered systems in the presence of ISA in R-space - upper panel: FT magnitude (solid line), fit magnitude (open circles), FT real part (thin solid line) and fit real part (open triangles); lower panel: Fourier-filtered data (solid line), raw data (thin solid line), back-transformed fit (open circles).

presence of colloids might represent a relevant contribution to the overall solubility measured by Moreton and co-workers.

The collected data in HQ-buffered systems at $pH_m = 8$ (Fig. 3 b) and 11 (c) also display a $m(Pu)_{tot}$ *vs.* $m(ISA)_{tot}$ slope of ~ +1, suggesting that the Pu:ISA stoichiometric ratio of the complex at $pH_m < 12$, is again 1. Together with the data obtained at pH_m = constant = 12 and $m(ISA)_{tot} = 10^{-6} - 0.1$ m, the gained results give a consistent picture of the Pu–ISA speciation scheme, supporting the participation of one ISA molecule in the complex formation reaction with Pu(IV) within the entire, $8 \leq pH_m \leq 13$ range. As solubility experiments in Sn(II)-systems with varying ISA concentration were only performed for $pH_m = 12$ condition, the formation of complexes with Pu(III):ISA = 1 at $pH_m < 12$ under strongly reducing conditions remains only as a (plausible) hypothesis.

4.1.3. Solid phase characterization

4.1.3.1. Synchrotron-based in-situ XRD. Fig. 4 shows the *in-situ* XRD patterns of the solid phases controlling the solubility of Pu in HQ and Sn (II) systems, equilibrated in solutions with $m(ISA)_{tot} = 10^{-3}$ m at $pH_m = 9$, or with $m(ISA)_{tot} = 0.10$ m at $pH_m = 12$. In all cases, the equilibration time was 260 days. The figure also shows the diffractogram of the empty double polymeric containment used in the synchrotron-based measurements at the INE–Beamline as described in section 3.5.

All diffractograms in Fig. 4 (corresponding to Pu solid phases) contain XRD reflections that perfectly match with the reference pattern of PuO_2(cr) reported in Zachariansen (1949). A large number of additional signals are also observed in the Sn(II) system at $pH_m = 9$, as expected. The latter show a moderate agreement with $Sn_6O_4(OH)_4$(cr) (PDF 14–0140) and SnO(cr) (PDF 13–0111) (Wong-Ng et al., 2001), which are the likely solid phases controlling the solubility of Sn(II) at this pH_m (Gamsjäger et al., 2012). The lack of reflexes corresponding to Sn(II) solid phases at $pH_m = 12$ is consistent with the significantly higher Sn(II) solubility at this pH_m owing to the formation of anionic Sn (II) hydrolysis species which leads to the total dissolution of the introduced Sn(II)-content.

4.1.3.2. XANES. Figure SI-5 (in Supporting Information) shows Pu L_{III}–edge XANES spectra collected for the solid phases controlling the solubility of Pu in HQ and Sn(II)-buffered solutions, with $m(ISA)_{tot} = 10^{-3}$ m at $pH_m = 9$ and $m(ISA)_{tot} = 0.10$ m at $pH_m = 12$ (t_{eq} = 260 days). The figure also includes XANES reference spectra of $Pu(III)_{aq}$ and $Pu(IV)_{aq}$ collected at the INE-Beamline and reported by Brendebach and co-workers (Brendebach et al., 2009).

The edge energies of the XANES spectra collected for all the retrieved Pu solid phases are in excellent agreement with the Pu(IV) reference spectrum reported by Brendebach and co-workers (Brendebach et al., 2009). Furthermore, the XANES spectra of the Pu solid phases equilibrated in ISA-containing solutions perfectly match the spectrum of the initial PuO_2(ncr,hyd) solid phase as well (designated as "starting material") collected in our previously study (Tasi et al., 2018).

4.1.3.3. EXAFS. The Fourier-transformed (FT) representation of the k^2-weighted EXAFS data depicted in Fig. 5 for HQ and Sn(II) systems (upper panel: FT magnitude, imaginary part and fit results in R-space, lower panel: raw data, Fourier-filtered data and fit results in k-space) corresponds to a radial pair distribution function uncorrected for photoelectron central and neighbour atom phase-shifts. Two coordination shells are discernible for all samples investigated in the present work: the first one around 1.75 Å (R − Δ) reflects Pu bonding to bridging oxygen atoms and to oxygen from terminal water and hydroxide units. These different oxygen neighbours exhibit a spread of bond distances generally leading to large Debye–Waller factors or requiring inclusion of an asymmetry parameter (3rd cumulant) in the fit - or even a second oxygen neighbour shell (*cf., e.g.* to Rothe et al. (2004)). The second shell around 3.6 Å (R − Δ) reflects backscattering from second next Pu neighbours in the solid precipitates. All metric parameters are listed in Table 1.

As observed in our previous Pu study in the absence of ISA (Tasi et al., 2018), all solids investigated in the present work show a fluorite type signature. No clear trends are observed with pH_m (9 and 12) or reducing agent (HQ and Sn(II)). In all cases, R_{Pu-O} scatters around 2.30 Å and R_{Pu-Pu} around 3.80 Å, whereas coordination numbers N_O scatters around 6 and N_{Pu} around 4. As extensively discussed in previous publications (Tasi et al., 2018), the nanocrystalline character of the PuO_2(ncr,hyd) material used in this work leads to a significantly distorted local order around individual Pu centres, which importantly reduces the coordination number reported for ideal fluorite-type PuO_2:

Table 1
Data range and metric parameters extracted by least-squares fitting of EXAFS spectra to the EXAFS equation.

Sample name	k-range [Å^{-1}] fit-range [Å]	shell	N	R [Å]	ΔE_0 [eV][a]	σ^2 [Å^2]	r-factor [%]
pH_m = 9, HQ	1.80 – 13.28	O	5.9	2.30	−0.44	0.0081	2.7
$m(ISA)_{tot} = 10^{-3}$ m	0.95 – 4.14	Pu	3.4	3.81		0.0021	
pH_m = 9, Sn(II)	1.75 – 13.46	O	6.6	2.28	−2.28	0.0081	2.4
$m(ISA)_{tot} = 10^{-3}$ m	0.98 – 4.11	Pu	4.3	3.78		0.0030	
pH_m = 12, HQ	1.70 – 13.29	O	5.9	2.30	−1.11	0.0082	6.6[b]
$m(ISA)_{tot}$ = 0.01 m	1.04 – 4.11	Pu	4.1	3.80		0.0030	
pH_m = 12, Sn(II)	1.75 – 13.47	O	5.2	2.29	−2.31	0.0060	1.6[c]
$m(ISA)_{tot}$ = 0.01 m	0.90 – 4.06	Pu	3.5	3.80		0.0025	

S_0^2 = 1.0 fixed (slightly underestimating N in all fits).
Errors: $R_{Pu\text{-}O}$ 0.01 Å, $R_{Pu\text{-}Pu}$ 0.02 Å.
[a] Global parameter for both shells.
[b] Worst fit in series, reason unclear, low frequency contribution not reproduced.
[c] Best fit in series.

R_{Pu-O} = 2.32 Å, N_O = 8; R_{Pu-Pu} = 3.81 Å, N_{Pu} = 12. This is attributed to destructive interference of the backscattered photoelectron waves.

In summary, experimental evidences from *in-situ*-XRD, XANES and EXAFS measurements unequivocally confirm that the initial material, nanocrystalline Pu(IV)O_2(ncr,hyd) remains stable and controls the solubility of Pu in all systems in the presence of ISA. This observation was considered in Section 4.2 for deriving chemical and thermodynamic models for the Pu–ISA system in HQ- and Sn(II)-buffered systems.

4.2. Thermodynamic description of the Pu–OH–ISA system

Chemical reactions 4, 7 and 10 are expected to control the solubility of Pu under alkaline reducing conditions and in the absence of ISA. The corresponding equations (5), (6); (8), (9) and (11), (12) were used in combination with stability constants and SIT ion interaction coefficients summarized in Table A1 and Table A2 of the Appendix to calculate the solubility lines in Figure 2, 3, 6, and 7: PuO_2(am,hyd) in equilibrium with $Pu(IV)_{aq}$ (black line, calculated using equilibrium constants reported in NEA-TDB (Guillaumont et al., 2003)); PuO_2(am,hyd) in equilibrium with $Pu(IV)_{aq}$ and $Pu(III)_{aq}$ at (pe + pH_m) = 1.54 (grey line); and $Pu(OH)_3$(am) in equilibrium with $Pu(III)_{aq}$ (light blue line). The solubility curve plotted for $Pu(OH)_3$(am) were calculated using log $^*K^\circ_{IIIs,0}$ = 14.58, as reported in Cho et al. (2016). These thermodynamic and activity models and accordingly calculated solubility lines are the basis for the thermodynamic description of the systems Pu(IV)–OH–ISA and Pu(III)–OH–ISA, which are derived in sections 4.2.1 and 4.2.2 based upon solubility data and solid phase characterization results discussed above.

$$Pu(III)(OH)_3(am) + n\ H^+ \Leftrightarrow Pu(III)(OH)_{3-n}^{n+} + n\ H_2O(l) \quad (4)$$

$$\log {}^*K^\circ_{IIIs,(3-n)} = \log {}^*K'_{IIIs,(3-n)} + \log \gamma_{Pu(III)(OH)3-n}{}^{n+} + n \log a_w - n \log \gamma_H{}^+ \quad (5)$$

$$\log {}^*K'_{IIIs,(3-n)} = \log m_{Pu(III)(OH)3-n}{}^{n+} + n\ pH_m \quad (6)$$

$$Pu(IV)O_2(am,hyd) + n\ H^+ \Leftrightarrow Pu(IV)(OH)_{4-n}^{n+} + (n-2)\ H_2O(l) \quad (7)$$

$$\log {}^*K^\circ_{IVs,(4-n)} = \log {}^*K'_{IVs,(4-n)} + \log \gamma_{Pu(IV)(OH)4-n}{}^{n+} + (n-2) \log a_w - n \log \gamma_H{}^+ \quad (8)$$

$$\log {}^*K'_{IVs,(4-n)} = \log m_{Pu(IV)(OH)4-n}{}^{n+} + n\ pH_m \quad (9)$$

$$Pu(IV)O_2(am,hyd) + (1+n)\ H^+ + e^- \Leftrightarrow Pu(III)(OH)_{3-n}^{n+} + (n-1)\ H_2O(l) \quad (10)$$

$$\log {}^*K^\circ_{IVs/III,(3-n)} = \log {}^*K'_{IVs/III,(3-n)} + \log \gamma_{Pu(III)(OH)3-n}{}^{n+} + pe + (n-1) \log a_w - (1+n) \log \gamma_H{}^+ \quad (11)$$

$$\log {}^*K'_{IVs/III,(3-n)} = \log m_{Pu(III)(OH)3-n}{}^{n+} + (1+n)\ pH_m \quad (12)$$

4.2.1. Chemical and thermodynamic model of the system Pu(IV)–OH–ISA

The solubility data obtained in HQ-buffered systems with m$(ISA)_{tot}$ < 0.10 m were used to derive the chemical and thermodynamic models for the Pu(IV)–ISA system. As demonstrated in our previous study (Tasi et al., 2018) and further confirmed in the present work, the use of HQ as a redox buffer stabilizes the +IV redox state of Pu in both aqueous and solid phases over the given pH range.

Based on the slope analyses depicted in Figs. 2 and 3 (log m$(Pu)_{tot}$ *vs.* pH_m and log m$(Pu)_{tot}$ *vs.* log m$(ISA)_{tot}$) and considering PuO_2(ncr,hyd) as the solid phase controlling the solubility of Pu(IV), chemical reactions 13 and 14 are proposed to control the solubility and solution chemistry of Pu(IV) in the presence of ISA within 8 ≤ pH_m ≤ 13.

$$Pu(IV)O_2(ncr,hyd) + ISA^- + 2\ H_2O(l) \Leftrightarrow Pu(IV)(OH)_4ISA^- \quad (13)$$

$$Pu(IV)O_2(ncr,hyd) + ISA^- + 3\ H_2O(l) \Leftrightarrow Pu(IV)(OH)_5ISA^{2-} + H^+ \quad (14)$$

The species $Pu(OH)_4ISA^-$ is predominant at pH_m = 8 – 11, whereas $Pu(OH)_5ISA^{2-}$ forms in systems with pH_m > 11. Note that the proposed stoichiometries for the Pu(IV)–ISA complexes assume highly hydrolysed Pu(IV) moieties ("$Pu(OH)_4$" and "$Pu(OH)_5^-$") coordinated to one ISA^- ligand where only the carboxylic group is deprotonated. This nomenclature is formally used in this section for the sake of consistency with previous studies, although the existence of the moiety "$Pu(OH)_5^-$" is highly unlikely and both $Pu(OH)_4ISA^-$ and $Pu(OH)_5ISA^{2-}$ possibly involve the deprotonation of one or several alcohol groups of ISA. An in-depth discussion of the structure of Pu(III/IV)–ISA complexes is provided in section 4.3 based upon DFT calculations. Note that in recent studies on the Zr(IV)–ISA (Kobayashi et al., 2017b) and U(IV)–ISA systems (Kobayashi et al., 2017a) under alkaline to hyperalkaline conditions, Kobayashi and co-workers proposed also the existence of highly hydrolysed moieties ("$Zr(IV)(OH)_5^-$" and "$U(IV)(OH)_5^-$") to explain the solubility behavior of Zr(IV) and U(IV) in the presence of ISA at pH_m > 12.

Data evaluation using the non-linear regression analysis method of least-squares involved the application of the following model function:

$$f(K'_{IVs,4+y1,x1} \ldots, K'_{IVs,4+yi,xi}) = (\Sigma\ {}^{n}_{i=1}[(\log m^{exp,n}_{Pu,tot} - \log m^{calc,n}_{Pu,tot})^2])^{0.5} \cdot (n-1)^{-1}, \quad (15)$$

where $m^{exp,n}_{Pu,tot}$ is the experimentally determined total concentration of Pu in solution and n is the number of data points. The parameters $^*K'_{IVs,4+yi,\ xi}$ (with i = 1, 2) are the conditional equilibrium constants (at I = 0.10 m NaCl) corresponding to the solubility reactions 13 and 14, which can be expressed as indicated in equation (16):

$$\log {}^*K'_{IVs,4+y,x} = \log m_{Pu(IV)(OH)4+y(ISA)x}{}^{-(x+y)} + y \log m_H{}^+ - x \log m_{ISA}{}^-, \quad (16)$$

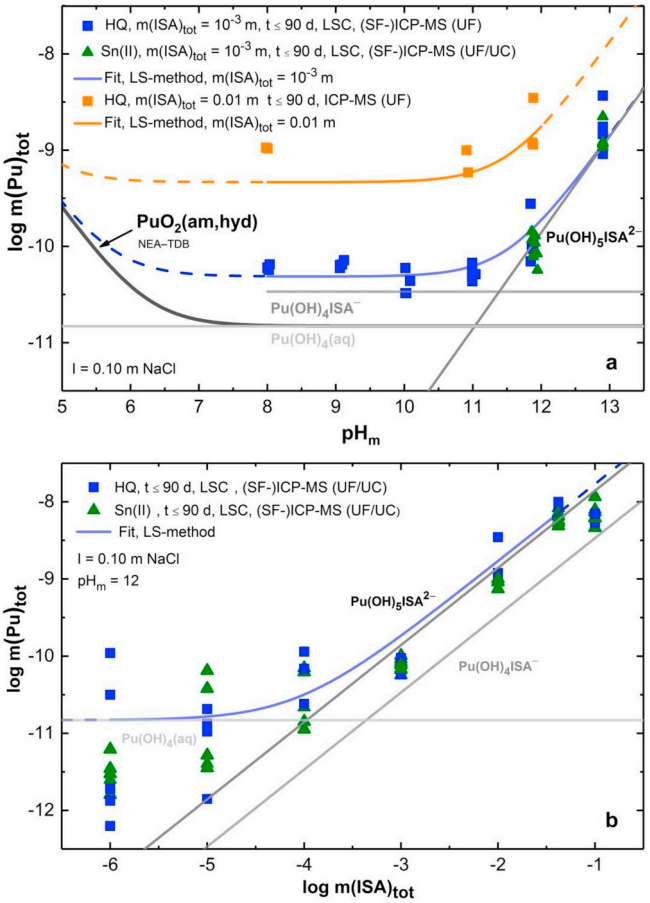

Fig. 6. Experimentally measured $m(Pu)_{tot}$ in equilibrium with PuO_2(ncr,hyd) at I = 0.10 m NaCl in HQ-buffered systems **a**, with pH_m = 8–12.9 in the presence of $m(ISA)_{tot} = 10^{-3}$ m (■) and 0.01 m (▲) and in Sn(II)-buffered systems (■), at $pH_m > 11$ with $m(ISA)_{tot} = 10^{-3}$ m or **b**, at constant $pH_m = 12$ with 10^{-6} m ≤ $m(ISA)_{tot}$ = 0.10 m. Solubility lines (solid and dashed) in blue (with $m(ISA)_{tot} = 10^{-3}$ m or at pH_m = 12) and in orange (with $m(ISA)_{tot}$ = 0.01 m) for $Pu(IV)O_2$(ncr,hyd) in the presence of ISA are calculated (at I = 0.10 m NaCl) using the chemical and thermodynamic models derived in this work. Black solid line corresponds to the thermodynamically calculated solubility of PuO_2(am,hyd) in the absence of ISA. UF and UC indicate the use of ultrafiltration and ultracentrifugation as phase separation methods. (For interpretation of the references to colour in this figure legend, the reader is referred to the Web version of this article.)

where y = 0 ($Pu(OH)_4ISA^-$; $\log {}^*K'_{IVs,4,1}$) or 1 ($Pu(OH)_5ISA^{2-}$; $\log {}^*K'_{IVs,5,1}$).

The dependent variable $m^{calc,n}_{Pu,tot}$ is the total concentration of Pu in solution calculated according to equation (17) and considering the total concentration of ISA ($m(ISA)_{tot}$) with the experimentally measured pH_m (converted to m_{H^+}) value. Taking into account the significantly higher total concentrations of ISA compared to solubility of Pu, the free concentration of ISA in solution, m_{ISA^-}, was set equal to $m(ISA)_{tot}$.

$$m^{calc,n}_{Pu,tot} = \Sigma_{n=1}^{4} ({}^*K'_{IVs,(4-n)} (m_{H^+})^n) + \Sigma_{i=1}^{2} ({}^*K'_{IVs,4+yi,xi} (m_{ISA^-})^{xi} (m_{H^+})^{-yi}) \quad (17)$$

The SIMPLEX method (Nelder and Mead, 1965) was applied to minimize the objective function (equation (15) - the averaged square root of the sum of squared residuals). The optimized values of ${}^*K'_{IVs,4,1}$ and ${}^*K'_{IVs,5,1}$ were then extrapolated to $I \rightarrow 0$ using equation (18) and SIT ion interaction coefficients with the values of $\varepsilon(Pu(OH)_4ISA^-; Na^+) = -(0.05 \pm 0.10)$ kg·mol^{-1} and $\varepsilon(Pu(OH)_5ISA^{2-}; Na^+) = -(0.10 \pm 0.10)$ kg·mol^{-1}, estimated according to empirical correlations with the charge of the complex as described by Hummel (2009):

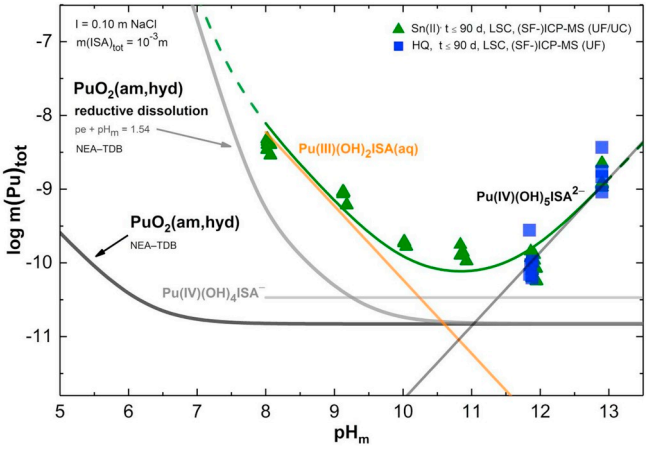

Fig. 7. Experimentally measured $m(Pu)_{tot}$ in equilibrium with PuO_2(ncr,hyd) at I = 0.10 m NaCl in Sn(II)-buffered systems (■) with pH_m = 8–12.9 in the presence of $m(ISA)_{tot} = 10^{-3}$ m and in HQ-buffered systems (■), at $pH_m > 11$ with $m(ISA)_{tot} = 10^{-3}$ m. Solubility curves (solid and dashed) in green (with m $(ISA)_{tot} = 10^{-3}$ m) for $Pu(IV)O_2$(ncr,hyd) in the presence of ISA are calculated (at I = 0.10 m NaCl) using the chemical and thermodynamic models derived in this work. Black and grey solid lines correspond to the thermodynamically calculated solubility of PuO_2(am,hyd) in the absence of ISA, calculated using equilibrium constants reported in the NEA-TDB (Guillaumont et al., 2003). (For interpretation of the references to colour in this figure legend, the reader is referred to the Web version of this article.)

$$\log {}^*K^\circ_{IVs,4+y,x} = \log {}^*K'_{IVs,4+y,x} + \log \gamma_{Pu(IV)(OH)4+y(ISA)x}{}^{-(x+y)} + y \log \gamma_{H^+} - x \log \gamma_{ISA^-} - y \log a_w \quad (18)$$

As a last step, the resulting solubility constants $\log {}^*K^\circ_{s,4,1}$ and $\log {}^*K^\circ_{s,5,1}$ were converted (in accordance with chemical equation (19)) into the corresponding formation constants $\log {}^*\beta^\circ_{1,4,1}$ and $\log {}^*\beta^\circ_{1,5,1}$ using $\log {}^*K^\circ_{IVs,0}[PuO_2(am, hyd)] = -(58.33 \pm 0.52)$ as selected in the NEA-TDB (Guillaumont et al., 2003). The latter value is in excellent agreement with $\log {}^*K^\circ_{IVs,0}[PuO_2(ncr,hyd)]$ determined in our previous study (Tasi et al., 2018) for the same solid phase used in the present work:

$$Pu^{4+}(aq) + x\ ISA^- + (4 + y)\ H_2O(l) \Leftrightarrow Pu(IV)(OH)_{4+y}ISA^{-(x+y)} + (4 + y)\ H^+ \quad (19)$$

$$\log {}^*\beta^\circ_{1,4+y,x} = \log a_{Pu(IV)(OH)4+y(ISA)x}{}^{-(x+y)} + (4 + y) \log a_{H^+} - \log a_{Pu}{}^{4+} - x \log a_{ISA^-} - (4 + y) \log a_w \quad (20)$$

To validate the modeling approach described above, an independent data evaluation was also performed using the PHREEPLOT-PHREEQC (PP–PQC) program packages (see also section 3.6). For this purpose, a database was prepared containing all necessary equilibrium constants and SIT ion interaction coefficients (including $\varepsilon(Pu(OH)_4ISA^-; Na^+)$ and $\varepsilon(Pu(OH)_5ISA^{2-}; Na^+)$) as summarized in Table A1 and Table A2 of the Appendix. With this database, the PhreePlot software was used to optimize the values of $\log {}^*\beta^\circ_{1,4,1}$ and $\log {}^*\beta^\circ_{1,5,1}$. The applied objective function was the averaged square root of the sum of squared residuals (corresponding to the parameters to be optimized). The refinement of the defined cumulative equilibrium constants (as in equation (20), at I = 0) was combined with the internal calculation of the ionic strength, based upon the initially set m(NaCl), $m(ISA)_{tot}$ and pH_m values. The modified Levenberg-Marquardt procedure (Powell, 1965) implemented in PP–PQC was used in the optimization process.

Table 2 shows the values of $\log {}^*\beta^\circ_{1,4,1}$ and $\log {}^*\beta^\circ_{1,5,1}$ obtained with the two different data evaluation approaches used. The nearly identical results in both approaches provide further confidence in the optimized $\log {}^*\beta^\circ_{1,4,1}$ and $\log {}^*\beta^\circ_{1,5,1}$ values. Because of the higher internal consistency and the more accurate calculation of ionic strength, the result

Table 2
Modeling results for the equilibrium constants (at I = 0, as expressed in equation (20) for $Pu(OH)_4ISA^-$ with $\log {}^*\beta^\circ_{1,4,1}$ and $Pu(OH)_5ISA^{2-}$ with $\log {}^*\beta^\circ_{1,5,1}$) obtained with the non-linear regression analysis method of least–squares (LS–method) or with the PHREEPLOT-PHREEQC software package (PP–PQC).

$\log {}^*\beta^\circ_{1,4+y,1}$	Parameters of evaluated data sets (HQ system)		Approach	Modeling results
$Pu(IV)(OH)_{4+y}ISA^{-(1+y)}$	$m(ISA)_{tot}$ [m]	pH_m		(I → 0 m)
$\log {}^*\beta^\circ_{1,4,1}$	< 0.10	8 – 12.9	LS	−5.03
$\log {}^*\beta^\circ_{1,5,1}$	< 0.10	8 – 12.9	LS	−16.98
$\log {}^*\beta^\circ_{1,4,1}$	< 0.10	8 – 12.9	PP–PQC	**–(5.03 ± 0.12)**
$\log {}^*\beta^\circ_{1,5,1}$	< 0.10	8 – 12.9	PP–PQC	**–(16.92 ± 0.13)**

obtained with PP–PQC is taken as the final set of thermodynamic constants and uncertainties for the Pu(IV)–ISA system.

The solubility of $Pu(IV)O_2$(ncr,hyd) in the presence of ISA calculated using the chemical and thermodynamic models derived in the present work are shown in Fig. 6 along with the corresponding experimental data sets obtained in this study. For comparison, the figure also includes experimental solubility data obtained in Sn(II) systems with pH_m > 11.

Fig. 6 shows that the solubility of $Pu(IV)O_2$(am,hyd) in the presence of ISA calculated using the chemical and thermodynamic models derived in this work are in excellent agreement with the experimentally measured solubility in HQ systems. Although experimental data obtained in Sn(II) systems were not used for the refinement of the parameters, chemical and thermodynamic models derived from HQ systems properly explain solubility data in Sn(II) systems at pH_m > 11. This observation strongly suggests that the chemical reaction controlling the solubility of Pu is the same in both systems under the outlined conditions, *i.e.* PuO_2(ncr, hyd) ⇔ Pu(IV)–ISA(aq).

4.2.2. Chemical and thermodynamic model of the system Pu(III)-OH-ISA

Based on solubility data and solid phase characterization discussed in sections 4.1.2.1 and 4.1.3, respectively, the reductive dissolution equilibrium $Pu(IV)O_2$(ncr,hyd) + e^- ⇔ Pu(III)–ISA(aq) is proposed to control the solubility of Pu in the Sn(II)-buffered systems at pH_m = 8 – 11. Consequently, the definition of chemical and thermodynamic models for this system requires accounting for the redox potential (as pe or rather the (pe + pH_m) values) within these boundary conditions.

As discussed in section 4.1.1, a constant value of (pe + pH_m) = (1.54 ± 0.14) was considered in the following thermodynamic evaluation. The slope analysis discussed in section 4.1.2.1 (with a log m $(Pu)_{tot}$ *vs.* pH_m slope of −1) accordingly can be interpreted with the predominance of Pu(III)–ISA aqueous complex with Pu(III):OH ratio 1:2 as ex in equation (21):

$$Pu(IV)O_2(ncr,hyd) + 2\,H^+ + x\,ISA^- + e^- \Leftrightarrow Pu(III)(OH)_2ISA_x^{-x} + H_2O\,(l) \quad (21)$$

The number of ISA molecules (x) in the complex $Pu(III)(OH)_2ISA_x^{-x}$ cannot be derived from the solubility data obtained in the present work and was assumed to be 'one' in analogy to the Pu(IV)–ISA complexes discussed in section 4.2.1, *i.e.* Pu(III)$(OH)_2$ISA(aq). The possible formation of additional complexes with Pu(III):OH:ISA stoichiometries 1:1:1 and 1:3:1 was also evaluated and the quality of the fit was compared in terms of $\Delta\Sigma(\sigma^2)$. As in the case of Pu(IV)–ISA complexes, note again that isomeric Pu(III)–ISA complex/es can be defined by modifying the number of hydroxide ions and the deprotonated hydroxyl functional groups on the ISA ligand coordinated to the Pu^{3+} ion. In this section, the hydrolysis of the metal ion is initially assumed, although a detailed discussion on the structure of this complex is provided later, in section 4.3.

The quantitative analysis of solubility data was performed using the non-linear regression analysis method of least-squares described in section 4.2.1 (LS–method, see equation (15)). The optimized parameter was the conditional equilibrium constant ($^*\beta'_{1,2,1}$; at I = 0.10 m NaCl) corresponding to reaction 22 and related equation (23).

$$Pu^{3+}(aq) + ISA^- + 2\,H_2O(l) \Leftrightarrow Pu(III)(OH)_2ISA(aq) + 2\,H^+ \quad (22)$$

$$\log {}^*\beta^\circ_{1,2,1} = \log a_{Pu(III)(OH)2ISA(aq)} + 2\log a_{H^+} - \log a_{Pu^{3+}} - \log a_{ISA^-} - 2\log a_w \quad (23)$$

Equation (24) was used to calculate the total concentration of Pu in solution ($m^{calc,n}_{Pu,tot}$). Free ISA concentration, m_{ISA^-}, was set equal to m $(ISA)_{tot}$. The value of $^*K'_{IVs/III,(3-n)}$ corresponding to the reductive dissolution of PuO_2(am, hyd) was calculated by combining pe with experimental pH_m using the value of (pe + pH_m) = 1.54 as discussed in section 4.1.1. The contribution of Pu(IV)–OH–ISA complexes to $m^{calc,n}_{Pu,tot}$ was accounted for with $^*K'_{IVs,4,1}$ and $^*K'_{IVs,5,1}$ which were calculated for I = 0.10 m NaCl using the thermodynamic and activity models described in section 4.2.1. As for Pu(IV)–OH–ISA complexes, minimization of the objective function (optimization of $^*\beta'_{1,2,1}$) was performed with the SIMPLEX method (Nelder and Mead, 1965).

$$m^{calc,n}_{Pu,tot} = \Sigma_{n=1}^{4}({}^*K'_{IVs,(4-n)}\,(m_{H^+})^n) + \Sigma_{n=1}^{3}({}^*K'_{IVs/III,(3-n)}\,(m_{H^+})^n) + \Sigma_{i=1}^{2}({}^*K'_{IVs,4+yi,xi}\,(m_{ISA^-})^{xi}\,(m_{H^+})^{-yi}) + {}^*\beta'_{1,2,1}\,(m_{ISA^-})\,(m_{Pu^{3+}})\,(m_{H^+})^{-2} \quad (24)$$

The optimized value of $^*\beta'_{1,2,1}$ was extrapolated to reference state, I → 0, using equation (25), where the SIT ion interaction coefficient was $\varepsilon(Pu(OH)_2ISA(aq); Na^+/Cl^-) = 0.00\,kg{\cdot}mol^{-1}$, as given by definition for neutrally charged species in the SIT formalism.

$$\log {}^*\beta^\circ_{1,2,1} = {}^*\beta'_{1,2,1} + \log \gamma_{Pu(III)(OH)2ISA(aq)} + 2\log \gamma_{H^+} - \log \gamma_{ISA^-} - 2\log a_w \quad (25)$$

The overall evaluation of the experimental data did not improve significantly when including the species 1:1:1 and 1:3:1 ($\Delta\Sigma(\sigma^2)$ < 1%, compared to the case with only Pu(III)$(OH)_2$ISA(aq)), and thus the existence of a second Pu(III)–ISA complex within the boundary conditions of this study was finally disregarded.

As for the system Pu(IV)–OH–ISA, the value of $^*\beta^\circ_{1,2,1}$ was also optimized with the PP–PQC program package. The procedure was executed just as described in section 4.2.1, although in the present case measured redox potentials (as pe values) were also taken in consideration as second independent variables. Two different approaches were used in the PP–PQC optimization. In the first one, uncertainty was calculated as 3σ of the overall fit, which however, does not account for the uncertainty of the independent variables (collected pe and pH_m values). In the second approach, Monte Carlo simulations were used to generate new sets of pe and log $m(Pu)_{tot}$ input values randomly scattered (following Gaussian distribution) around the respective mean values. A total of 2000 new data sets were generated and independently re-modelled with PP–PQC. This approach aims to reflect the uncertainty associated with pe values, and thus provides an improved description of the overall uncertainty in the thermodynamic constants. A detailed description of this approach is provided in section SI-6 (in Supporting Information).

Table 3 shows the optimized values of log $^*\beta^\circ_{1,2,1}$ obtained with LS and PP–PQC approaches. Note that both values overlap with each other if considering the uncertainty calculated with the Monte Carlo method. The result obtained with the PP–PQC approach has been favoured as in the case of the Pu(IV)–ISA–OH system.

Fig. 7 shows the solubility of $Pu(IV)O_2$(ncr,hyd) in the presence of ISA under strongly reducing conditions (pe + pH_m = 1.54) calculated using the chemical and thermodynamic models derived in the present work, along with the corresponding experimental data sets obtained in Sn(II)-buffered systems. For comparison, Fig. 7 also includes experimental solubility data obtained in HQ systems at pH_m > 11. The excellent agreement between the calculated and all measured log $m(Pu)_{tot}$

Table 3
Evaluation of the equilibrium constant $\log^{*}\beta^{\circ}_{1,2,1}$ (for $I \rightarrow 0$, as expressed in equation (23)) obtained through the non-linear regression analysis method of least–squares (LS–method) or the PHREEPLOT–PHREEQC software package (PP–PQC).

Parameters of evaluated data sets (Sn(II) system)		Evaluation approach	$\log^{*}\beta^{\circ}_{1,2,1}$ (I → 0)	Uncertainty estimation
$m(ISA)_{tot}$ [m]	pH_m			
10^{-3}	8 – 12.9	LS–method	−10.74	–
10^{-3}	8 – 12.9	PP–PQC	–(10.97 ± 0.10)	" ± 3σ"
10^{-3}	8 – 12.9	PP–PQC	**–(10.97 ± 0.28)**	**"Monte Carlo"**

provides further confidence in the parameters optimized in this section for $pH_m \leq 11$.

4.3. Quantum chemical calculations

4.3.1. $Pu(IV)(OH)_4ISA^-$ and $Pu(IV)(OH)_5ISA^{2-}$ complexes

Based on experimental observations, the complexes $Pu(IV)(OH)_4ISA^-$ and $Pu(IV)(OH)_5ISA^{2-}$ were proposed in section 4.2.1 to dominate the aqueous speciation of Pu(IV) in HQ systems with m $(ISA)_{tot} \geq 10^{-3.5}$ m and $8 \leq pH_m \leq 13$. Slope analysis of solubility data provides only information on the stoichiometry of these complexes, in terms of Pu:OH:ISA ratio.

DFT calculations summarized in this section allow a further insight into the structure of these complexes, with focus on the hydrolysis of Pu^{4+} *vs.* deprotonation of hydroxyl functional groups (-OH) of the ISA molecule. Because of the aqueous character of the complexes under investigation and as a simplified model for the solvent, a number of water molecules were included in the calculations (i) saturating the hydroxyl functional groups of ISA and (ii) close to the metal ion in the first coordination shell of Pu^{4+}. Additional, a total of 8 water molecules were considered in a first approach, 4 by the ISA molecule and 4 in the first coordination shell of Pu^{4+}. In a second step, DFT + COSMO was applied to investigate the structure of the species in solution.

For both complexes under investigation, 8 oxygen atoms (belonging to ISA, water or to an OH^- ion) coordinated to Pu^{4+} in its first coordination shell. Previous CASPT2 calculations have shown that coordination numbers of 8 and 9 are energetically similar for Pu(IV) (Banik et al., 2014). Whilst keeping the charge of the complex constant, several configurations involving different number of hydroxide ions and deprotonated hydroxyl functional groups (alcoholate groups) of ISA (-C-O^-) were attempted: (i). $Pu(IV)(OH)_4ISA^-$, $Pu(IV)(OH)_3ISA_{-H}^-$, $Pu(IV)(OH)_2ISA_{-2H}^-$ and $Pu(IV)(OH)ISA_{-3H}^-$; (ii) $Pu(IV)(OH)_5ISA^{2-}$, $Pu(IV)(OH)_4ISA_{-H}^{2-}$, $Pu(IV)(OH)_3ISA_{-2H}^{2-}$ and $Pu(IV)(OH)_2ISA_{-3H}^{2-}$, where ISA_{-xH} corresponds to an ISA molecule with *x* deprotonated hydroxyl functional groups. In each case, several starting geometries were probed to ascertain that a reasonable local minimum was found for the calculated structures. This procedure was carried out both with and without the approximation of the aqueous solution phases with COSMO.

For the complex "$Pu(IV)(OH)_4ISA^-$", calculations with and without COSMO indicate that the α-OH group of ISA (on the second carbon, adjacent to the carboxylate group, see Fig. 8 a) is deprotonated (labelled as ISA(C2) in Table 4). ISA coordinates via the deprotonated α-OH and the -COO^- group with Pu(IV). Additionally, 3 -OH groups and 3 water molecules remain in the first coordination shell of the Pu(IV) ion. The same is observed for the "$Pu(IV)(OH)_5ISA^{2-}$" complex, although in this case the hydroxyl functional group of the fourth carbon atom (γ-OH, labelled as ISA(C4) in Table 4) was also deprotonated and this interacts directly with Pu(IV), leading to the removal of one water molecule from the first coordination shell of Pu(IV). The resulting structures optimized by DFT can be described as $Pu(IV)(OH)_3ISA_{-H}^-$ and $Pu(IV)(OH)_3ISA_{-2H}^{2-}$ (Fig. 8 a and b, respectively). For both complexes, we found through DFT calculations that a total of eight O-/O ions/atoms are located in the first coordination shell of the central metal ion.

Selected interatomic distances calculated by DFT and DFT + COSMO for the optimized structures of $Pu(IV)(OH)_3ISA_{-H}^-$ and $Pu(IV)(OH)_3ISA_{-2H}^{2-}$ are provided in Table 4. Expectedly, shorter distances are found in the complex $Pu(IV)(OH)_3ISA_{-H}^-$ for Pu(IV)–OH^- (average 232 pm/231 pm for DFT/DFT + COSMO) and Pu(IV)–ISA(-C2-O^-) (average 231 pm/230 pm), compared to the longer distances calculated for Pu(IV)–ISA(-COO^-) (239 pm/240 pm) and Pu(IV)–H_2O (259 pm/259 pm). Similar but in overall, slightly longer distances are obtained in the case of $Pu(IV)(OH)_3ISA_{-2H}^{2-}$, with average distances Pu(IV)–OH^- (233 pm/233 pm), Pu(IV)–ISA(-C4-O^-) (233 pm/232 pm), Pu(IV)–ISA(-C2-O^-) (240 pm/237 pm), Pu(IV)–ISA(-COO^-) (248 pm/249 pm) and Pu(IV)–H_2O (265 pm/261 pm). The larger interatomic distances in $Pu(IV)(OH)_3ISA_{-2H}^{2-}$ reflect the increased electronic density around the Pu^{4+} ion as a result of the additional coordination of the -C4-O^- of ISA. The highly coordinating environment around Pu^{4+}, with 5 and 6 "-O^-" groups (as OH^-, -C*n*-O^- and -COO^-) is also responsible for the increased Pu(IV)–H_2O and Pu(IV)–OH^- distances compared to values reported in the literature, e.g. $d(Pu^{4+}–OH_2) = (239 \pm 1)$ pm (Neck and Kim, 2001) and $d(Pu^{4+}–OH^-) = r_{Pu4+} + r_{OH-} = 101 + 122 = 223$ pm (Gaona et al., 2012; Neck and Kim, 2001).

4.3.2. $Pu(III)(OH)_2ISA(aq)$ complex

The same approach as described in the previous section was used in the optimization of the structure of the $Pu(III)(OH)_2ISA(aq)$ complex. In this case as well, several isomeric configurations with the same charge were evaluated: $Pu(III)(OH)_2ISA(aq)$, $Pu(III)(OH)ISA_{-H}(aq)$ and $Pu(III)ISA_{-2H}(aq)$. Both DFT and DFT + COSMO resulted in $Pu(III)(OH)ISA_{-H}(aq)$ as the energetically favoured configuration. The optimized structure and resulting Pu–O distances are provided in Fig. 8 c and Table 4, respectively.

Pu–O distances summarized in Table 4 for the complex $Pu(III)(OH)ISA_{-H}(aq)$ are systematically longer than the Pu(IV) counterparts, consistently with differences in the ionic radii of Pu^{4+} (101 pm for CN = 9) and Pu^{3+} (112 pm for CN = 8) (Neck and Kim, 2001) and the reduced charge at the metal ion. The distance calculated for Pu(III)–ISA(-COO^-) (251 pm) is in line with distances Cm(III)–L(-COO^-) reported in the literature for L = oxalate (239 – 251 pm) (Skerencak-Frech et al., 2015) and succinate (236 – 247 pm) (Frohlich et al., 2016) with side-on coordination mode, considering also differences in size between Pu^{3+} (112 pm) and Cm^{3+} (109 pm) ions (Neck and Kim, 2001).

4.4. Complexation of An(III/IV) with ISA under alkaline conditions: thermodynamic data derived in this work

Table 5 summarizes the equilibrium constants derived in the present work for the formation of Pu(III)–OH–ISA and Pu(IV)–OH–ISA complexes in alkaline to hyperalkaline pH_m conditions. Table 6 lists SIT ion interaction coefficients estimated for these complexes. Stoichiometry of these chemical reactions is provided by the combination of solubility data and solid phase characterization, whereas chemical formulae for Pu(III/IV)–OH–ISA complexes is based upon DFT calculations.

Chemical and thermodynamic models derived in this work provide the most accurate description available to date for the solubility of Pu in the presence of ISA. Thermodynamic data provided by Moreton et al. (2000) are clearly superseded by the more accurate control of the experimental conditions achieved in the present study (especially in terms of phase separation and E_h), as well as for the systematic variation of pH_m. The latter parameter was kept constant in the study by Moreton et al., and thus the stoichiometry of the complexes proposed by the authors remains speculative.

Fig. 9 a and b show the Pourbaix diagrams of Pu aqueous species in the presence of $\log m(ISA)_{tot} = -4$ and -2, respectively, calculated for

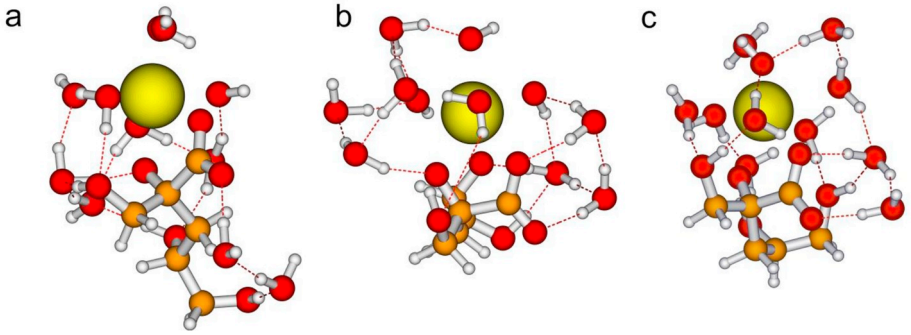

Fig. 8. Structures of the complexes (a) $Pu(IV)(OH)_3ISA_{-H}^-$ ("$Pu(IV)(OH)_4ISA^-$" in section 4.2.1) and (b) $Pu(IV)(OH)_3ISA_{-2H}^{2-}$ ("$Pu(IV)(OH)_5ISA^{2-}$" in section 4.2.1) and $Pu(III)(OH)ISA_{-H}(aq)$ ("$Pu(III)(OH)_2ISA(aq)$" in section 4.2.2), as optimized in this work by DFT calculations with and without COSMO.

Table 4
Pu–O distances (in pm) calculated by DFT and DFT + COSMO for the complexes $Pu(IV)(OH)_3ISA_{-H}^-$, $Pu(IV)(OH)_3ISA_{-2H}^{2-}$ and $Pu(III)(OH)ISA_{-H}(aq)$ as optimized in this work.

$Pu(IV)(OH)_3ISA_{-H}$–					
bond	DFT	+COSMO	bond	DFT	+COSMO
Pu(IV)–OH^-	226	227	Pu(IV)–ISA(-COO–)	239	240
Pu(IV)–ISA(-C2-O^-)	231	230	Pu(IV)–OH_2	250	251
Pu(IV)–OH^-	233	233	Pu(IV)–OH_2	260	259
Pu(IV)–OH^-	236	234	Pu(IV)–OH_2	267	267
$Pu(IV)(OH)_3ISA_{-2H}^{2-}$					
Pu(IV)–OH^-	227	230	Pu(IV)–ISA(-C2-O^-)	240	237
Pu(IV)–ISA(-C4-O^-)	233	232	Pu(IV)–ISA(-COO^-)	248	249
Pu(IV)–OH^-	234	235	Pu(IV)–OH_2	264	260
Pu(IV)–OH^-	237	235	Pu(IV)–OH_2	266	261
$Pu(III)(OH)ISA_{-H}(aq)$					
Pu(III)–ISA(-C2-O^-)	232	235	Pu(III)–OH_2	262	259
Pu(III)–OH^-	242	243	Pu(III)–OH_2	265	261
Pu(III)–ISA(-COO^-)	249	251	Pu(III)–OH_2	266	263
Pu(III)–OH_2	261	259	Pu(III)–OH_2	266	264

Table 5
Chemical equilibria and related equilibrium constants (for $I \rightarrow 0$ m) derived in the present study for the Pu(III/IV)–OH–ISA system.

Chemical equilibria	$\log^*\beta^\circ$ ($I \rightarrow 0$)
$Pu^{4+} + ISA^- + 3\ H_2O(l) \Leftrightarrow Pu(IV)(OH)_3ISA_{-H}^- + 4\ H^+$	–(5.03 ± 0.12)
$Pu^{4+} + ISA^- + 3\ H_2O(l) \Leftrightarrow Pu(IV)(OH)_3ISA_{-2H}^{2-} + 5\ H^+$	–(16.92 ± 0.13)
$Pu^{3+} + ISA^- + 2\ H_2O(l) \Leftrightarrow Pu(III)(OH)ISA_{-H}(aq) + 2\ H^+$	–(10.97 ± 0.28)

Table 6
SIT ion interaction coefficients estimated for the Pu(III/IV)–ISA–OH species.

species i	species j	ε(i,j) [kg·mol^{-1}]
$Pu(IV)(OH)_3ISA_{-H}^-$	Na^+	–(0.05 ± 0.10) [a]
$Pu(IV)(OH)_3ISA_{-2H}^{2-}$	Na^+	–(0.10 ± 0.10) [a]
$Pu(III)(OH)ISA_{-H}(aq)$	Cl^-/Na^+	0.00 [b]

[a] Estimated values based on the work of Hummel (2009).
[b] Defined to be zero by definition within SIT formalism.

$m_{Pu} = 10^{-11}$ m and $I = 0.1$ m NaCl using the thermodynamic and (SIT) activity models derived in the present work. Note that Pu(IV)–ISA colloids were not included in the present thermodynamic model, although they may play a relevant role in the solution chemistry of Pu under alkaline conditions and presence of ISA.

Fig. 9 shows that the presence of ISA at $m(ISA)_{tot} \leq 10^{-4}$ m has a minor impact on the aqueous speciation of Pu, and the predominance of the complex $Pu(IV)(OH)_3ISA_{-2H}^{2-}$ is only predicted at $pH_m > 12$. On the other hand, at $m(ISA)_{tot} = 10^{-2}$ m, Pu(III/IV)–OH–ISA species become predominant within $9 \leq pH_m \leq 13$. At this $m(ISA)_{tot}$ and for $pH_m < 11.5$, the stability field of $Pu(III)_{aq}$ is slightly increased towards higher pe values compared to ISA-free systems. Above this pH_m, the complex $Pu(IV)(OH)_3ISA_{-2H}^{2-}$ becomes again predominant and is the only Pu–ISA complex forming above the border of water reduction. Note however that other Pu(III)–ISA complexes beyond $Pu(III)(OH)ISA_{-H}(aq)$ possibly form under hyperalkaline conditions and may modify the latter statement. For instance, the species $Eu(OH)_3ISA^-$ and $Am(OH)_3ISA^-$ (expectedly $Eu(OH)_2ISA_{-H}^-$ and $Am(OH)_2ISA_{-H}^-$) were proposed (Tits et al., 2002, 2005; Vercammen et al., 2001) to control the solution chemistry of Eu(III) and Am(III) in the presence of ISA at pH = 13.3.

4.4.1. *Comparison with thermodynamic data available in the literature and systematic trends for An(IV) and An(III)/Ln(III)*

Due to the absence of reliable thermodynamic data for the binary system Pu(IV)–ISA, the chemical and thermodynamic models derived in the present work are compared with data available for Np(IV)–ISA and Th(IV)–ISA (Fig. 10 a, b, c). In both cases, data obtained in undersaturation solubility studies for Np(IV) (Rai et al., 2003) (recalculated in Gaona et al. (2008)) and Th(IV) (Colàs, 2014; Rai et al., 2009) were preferred[2], although the thermodynamic data derived in Vercammen et al. (2001) for the Th(IV)–ISA system from sorption studies (with large discrepancies to the work of Rai et al. (2009) and also Colàs (2014)) are shortly discussed as well.

Fig. 10 (a, b, c, d) shows the predominance diagrams of Th(IV)–ISA, Np(IV)–ISA and Pu(IV)–ISA calculated for $-6 \leq \log m(ISA)_{tot} \leq -1$ and $9 \leq pH_m \leq 13$ with $I = 0.10$ m NaCl using the thermodynamic data derived in the present work (Table 5) and summarized in Table SI-1 (in Supporting Information) for Np(IV) and Th(IV). In spite of the clear insights gained by DFT on the structures of Pu(IV)–ISA complexes, for the sake of comparison with data reported in the literature, the notation assuming the hydrolysis of the An(IV) cation instead of the deprotonation of hydroxyl functional groups of the ISA ligand has been used in the predominance diagram of Pu (Fig. 10 d).

Fig. 10 (a, c, d) shows significant differences in the calculated aqueous speciation of Th(IV)–ISA, Np(IV)–ISA and Pu(IV)–ISA systems. Thermodynamic data derived in the present work suggest the predominance of the 1:1 complex in the Pu(IV)–ISA system with $pH_m < 11.5$ and $m(ISA)_{tot} > 10^{-3.5}$ m. On the contrary, thermodynamic calculations conducted for Th(IV) show the predominance of the 1:2 complex above $m(ISA)_{tot} = 10^{-3}$ m, whereas the Np(IV) case results in the predominance of the 1:1 complex for $m(ISA)_{tot} \leq 10^{-2}$ m, and the predominance of the complex 1:2 above this $m(ISA)_{tot}$. Such

[2] Note that Colàs performed solubility experiments from both over- and undersaturation conditions.

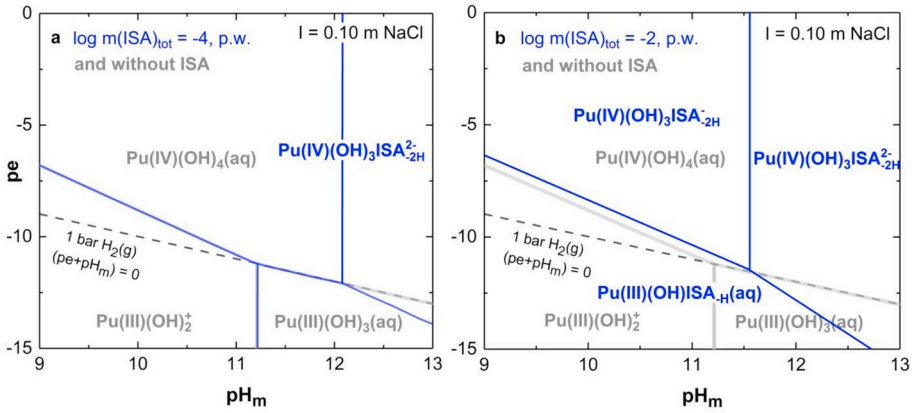

Fig. 9. Pourbaix diagram of Pu calculated for m $(Pu)_{tot} = 10^{-11}$ m and log $m(ISA)_{tot} = -4$: **a**, -2: **b**, (blue lines) and without ISA (grey lines) at $I = 0.1$ m NaCl using thermodynamic and (SIT) activity models as described in the text. Only aqueous species of Pu are shown in the diagram. Dashed lines correspond to the borderline of water reduction to $H_2(g)$ at $(pe + pH_m) = 0$. (For interpretation of the references to colour in this figure legend, the reader is referred to the Web version of this article.)

observations could be rationalized by differences in the size of the An^{4+} cation, with Th^{4+} and Pu^{4+} having the largest (1.08 ± 0.02 Å) and smallest (1.01 ± 0.02 Å) size, respectively (Neck and Kim, 2001). Hence, the formation of chelate complexes with An(IV):ISA ratio of 1:2 might be consequently favoured for the largest cation as steric repulsions between the coordinated ligands are less pronounced. However, as the uncertainties associated to these calculations are large and the number of An(IV)–ISA systems available are limited, the argumentation above does not represent any strong claim but must only be taken as a hypothesis.

The predominance diagram in Fig. 10 b calculated for the system Th(IV)–ISA using the equilibrium constants reported in Vercammen et al. (2001) shows a significantly different species distribution compared to Fig. 10 a. Calculations in Fig. 10 b predict the predominance of the species $Th(OH)_4ISA^-$ at $m(ISA)_{tot} \geq 10^{-5.9}$ m, whereas this species becomes only predominant at $m(ISA)_{tot} \geq 10^{-4.2}$ m in Fig. 10 a. Vercammen and co-workers did not report the formation of the 1:2 complex $Th(OH)_4(ISA)_2^{2-}$, which therefore does not appear in calculations shown in Fig. 10 b. Note, however that these authors conducted their experiments with $m(ISA)_{tot} \leq 10^{-2}$ m. The use of the speciation scheme and equilibrium constants in Fig. 10 b importantly overestimate experimental solubility data obtained from under- and oversaturation conditions in Rai et al. (2009) and in Colàs (2014). Although sorption experiments performed with ultra-trace concentrations of ^{228}Th or ^{234}Th may appear more susceptible to artefacts than solubility studies with macroscopic amounts of ^{232}Th, the discussion remains open and a final proof of concept for the proposed hypothesis is still missing.

Fig. 10 a, c, d also show significant differences in the aqueous speciation of the systems An(IV)–ISA as a function of pH_m. Both Np(IV)–ISA and Th(IV)–ISA show a pH-independent behavior of the aqueous speciation at $9 \leq pH_m \leq 13$, whereas the formation of the complex $Pu(OH)_5ISA^{2-}$ (or rather $Pu(OH)_3ISA_{-2H}^{2-}$) is predicted for the system Pu(IV)–ISA at $pH_m \geq 11.5$. Some relevant notes on these observations:

- Th(IV) solubility experiments in Rai et al. (2009) and in Colàs (2014) were performed at $pH_m \leq 12$. Consequently, these authors may simply have missed the formation of the complex "$Th(OH)_5ISA^{2-}$", which according to the Z_{eff} of Th(IV) may form at greater pH values.

- Due to differences in the ionic radii of the An^{4+} ions, the effective charges (Z_{eff}) of the An(IV) systems under consideration follow the pattern $Pu^{4+} \geq Np^{4+} > Th^{4+}$. Such differences are for instance responsible for the much weaker hydrolysis observed for Th^{4+}, compared to both Np^{4+} and Pu^{4+}. It can be hypothesized that differences in Z_{eff} are also responsible for the differences in the aqueous speciations of the Np(IV)–ISA and Pu(IV)–ISA systems.

- Np(IV) solubility experiments in Rai et al. (2003) were performed over a relatively short timeframe (≤ 20 days). A close inspection of their solubility data suggests that the authors may have not attained equilibrium conditions in their experiments. Hence, Fig. 5 in (Rai et al., 2003) shows systematic and very relevant differences (0.3 – 0.5 log-units) between solubility data at $t = 12$ days and $t = 20$ days (the latter showing systematically greater solubility). Solubility data reported at $pH_m = 13$ and 13.8 were only collected for t = 5 and 13 days (Fig. 4 in (Rai et al., 2003)). These experimental shortcomings may cast some doubts on the speciation scheme proposed by Rai and co-workers.

The discussion above does not provide a definitive explanation for the differences observed in the trends of An(IV)–ISA complexation with pH. In our view, the current study (using a combination of solubility studies including XAFS techniques and theoretical, DFT methods) in the system Pu(IV)–ISA represents the most comprehensive effort to characterize the systems and complexes forming under alkaline to hyperalkaline pH conditions. However, further experimental studies following a similar systematic and strategic approach as applied in the present work on the systems Th(IV)–ISA, U(IV)–ISA and Np(IV)–ISA would prove to be very helpful in understanding the overall picture of An(IV)–ISA complexation under conditions relevant for L/ILW disposal.

The only thermodynamic data available for the system An(III)–ISA under alkaline conditions was reported by Tits et al. (2005) for Am(III) based upon sorption experiments with calcite (see discussion in section SI-2.2). Experiments were performed only at pH = 13.3, and thus the stoichiometry of the complex forming ($Am(OH)_3ISA^-$) was proposed in analogy with Eu(III) (Vercammen et al., 2001).

Fig. 10 also displays the predominance diagrams of Am(III)–ISA (e) and Pu(III)–ISA (f) calculated for $-6 \leq \log m(ISA)_{tot} \leq -1$ and $9 \leq pH_m \leq 13$ at $I = 0.10$ m NaCl using the thermodynamic data derived in the present work (Table 5) and summarized in Table SI-1 (in Supporting Information) for Am(III).

Fig. 10 e and f shows different speciation schemes for Am(III)–ISA and Pu(III)–ISA systems, which basically reflect the experimental conditions in which the corresponding thermodynamic models were derived (pH = 13.3 for Am(III)–ISA in Tits et al. (2005), $pH_m \leq 11.5$ for Pu(III)–ISA in this work). Note further that the sorption study by Vercammen et al. (2001) on the system Eu(III)–ISA (basis for the chemical model proposed by Tits et al. (2005)) was performed at pH > 10.7, and thus these authors could not observe the formation of the complex $Eu(III)(OH)_2ISA(aq)$ proposed in the present work for Pu(III). Indeed, the combination of chemical and thermodynamic models available for Am(III)–ISA and Pu(III/IV)–ISA provides a satisfactory explanation of our solubility data in Sn(II) systems (see Figure SI-6 within Supporting Information). Although the incorporation of the species 1:3:1 in the fit of our solubility data did not result in a significant improvement of the fit (see section 4.2.2), the consideration of $\log {}^*\beta^\circ_{1,3,1} = -(21.4 \pm 1.0)$ as reported in Tits et al. for the chemical reaction $Am^{3+} + 3\ H_2O(l) + ISA^- \Leftrightarrow Am(OH)_3ISA^- + 3\ H^+$ can be considered as a reasonable upper limit also for the respective Pu(III) species. In the case of Pu(III), however, the predominance of this complex is limited to strongly alkaline and reducing conditions with $pH_m > 11.5$ and $(pe + pH_m) \leq 1.5$.

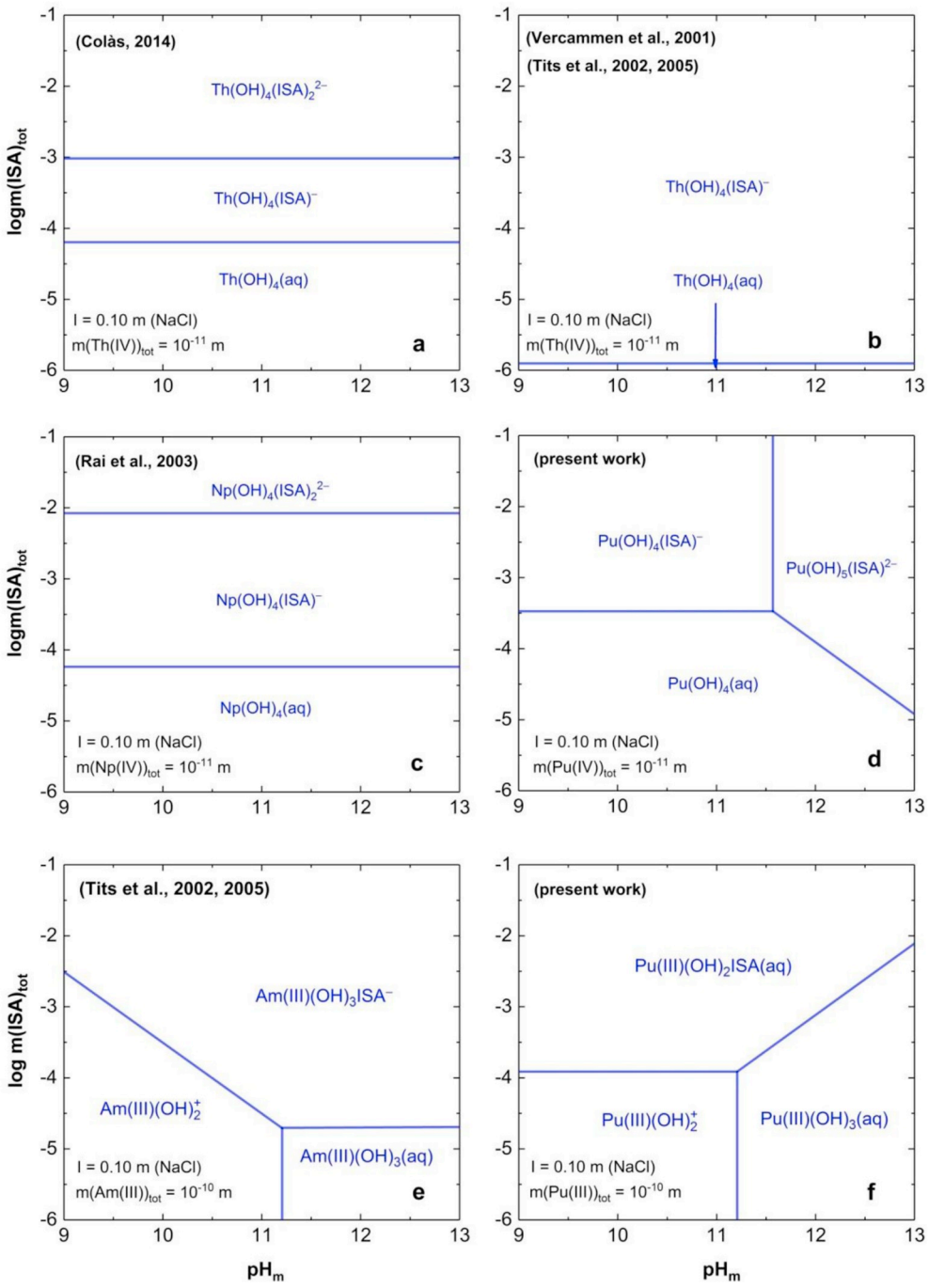

Fig. 10. Predominance diagrams of An(III/IV) in the presence of ISA ($-6 \le \log m(ISA)_{tot} \le -1$) with $m(An(IV))_{tot} = 10^{-11}$ m and $m(An(III))_{tot} = 10^{-10}$ m, $9 \le pH_m \le 13$ and $I = 0.10$ m NaCl, calculated for **a, Th (IV)** using thermodynamic data in Colàs (2014); **b, Th(IV)** using thermodynamic data in Vercammen et al. (2001), as recalculated in (Gaona et al., 2008); **c, Np(IV)** using thermodynamic data in Rai et al. (2003) as recalculated in (Gaona et al., 2008); **d, Pu (IV)** using thermodynamic data derived in the present work; **e, Am(III)** using thermodynamic data reported by Tits et al. (2002), (2005) and **b, Pu(III)** using thermodynamic data derived in the present work.

5. Summary and conclusions

The solubility and redox behavior of Pu under reducing conditions were comprehensively investigated in the presence of ISA, a polyhydroxycarboxylic acid resulting from the alkaline degradation of cellulose. A combination of solubility measurements, accurate control and monitoring of the redox conditions, extensive solid phase characterization and DFT calculations were used to identify the solid phases, aqueous species and chemical equilibria controlling the solubility of Pu at 10^{-6} m $\le m(ISA)_{tot} \le 0.1$ m and under (pe + pH_m) conditions relevant in the context of nuclear waste disposal.

In-situ XRD and XAS confirm that PuO_2(ncr,hyd) controls the solubility of Pu in all investigated systems, and that no reduction of the original Pu(IV) hydrous oxide takes place in the course of the experiments, even in very strongly reducing Sn(II)-buffered systems at (pe + pH_m) $\approx$ 1.5. ISA has a significant impact on the solubility of Pu under alkaline to hyperalkaline pH conditions at $m(ISA)_{tot} \ge 10^{-3.5}$ m, both in HQ and Sn(II) redox buffered systems. The observed effect is pH- and pe-dependent, thus involving the formation of Pu(IV)–ISA and Pu(III)–ISA aqueous complexes of varying Pu:OH ratio. Our results do not support the very high solubilities (up to $m(Pu)_{tot} = 10^{-3.5}$ m) previously reported for the system Pu(IV)–ISA. We hypothesize that such discrepancies arise from an insufficient phase separation in previous studies which can be ruled out in the present work. Indeed, our

experimental observations indicate that Pu–ISA colloids importantly contribute to the overall Pu concentration in equilibrium with PuO_2(ncr,hyd). Although this process cannot be parametrized in a thermodynamic model yet, it should be accounted for the estimation of realistic Pu solubility limits in NaCl media and absence of Ca(II).

Chemical and thermodynamic models derived for the system Pu(IV)–ISA were based on the new solubility experiments in HQ systems (after phase separation by ultrafiltration or ultracentrifugation) and detailed solid phase characterization. In combination with these experimental observations, DFT calculations suggest that α– and γ–OH groups of ISA deprotonate in the formation of a chelate with Pu(IV), and that $Pu(IV)(OH)_3ISA_{-H}^-$ and $Pu(IV)(OH)_3ISA_{-2H}^{2-}$ complexes predominate in solution. In Sn(II) systems with $pH_m < 11.5$, the combination of experimental data with theoretical calculations indicates that a reductive dissolution occurs with the predominance of the complex of $Pu(III)(OH)ISA_{-H}$(aq) in the aqueous phase.

This work provides robust solubility upper limits that allow estimating the source-term of Pu in alkaline reducing systems containing ISA. It further represents the most comprehensive thermodynamic dataset available to date for the system Pu^{3+}–Pu^{4+}–Na^+–OH^-–Cl^-–ISA^-–H_2O(l), which can be implemented in thermodynamic databases and geochemical calculations extending over a wide range of conditions relevant for nuclear waste disposal.

Acknowledgements

The research leading to this study was funded by SKB, the Swedish Nuclear Fuel and Waste Management Company. Additionally, the authors want to acknowledge the contribution of several colleagues from KIT-INE. The support received from Julian Schepperle and Christian Adam in the in-situ XRD and NMR measurements is highly appreciated. Frank Geyer and Annika Kaufmann are gratefully acknowledged for the (SF–)ICP–MS measurements. Thanks are due to Francesco Endrizzi as well for his support in the Monte-Carlo simulations.

Appendix

Table A1
Thermodynamic data used for the equilibrium calculations of Pu.

Reaction	Log K°
Redox processes	
$Pu^{3+} \leftrightarrow Pu^{4+} + e^-$	–(17.69 ± 0.04) [a]
$Pu^{3+} + 2\ H_2O(l) \leftrightarrow PuO_2(am,hyd) + 4\ H^+ + e^-$	–(15.36 ± 0.52) [a]
$Pu^{4+} + 2\ H_2O(l) \leftrightarrow PuO_2^+ + 4\ H^+ + e^-$	–(17.45 ± 0.69) [a]
$PuO_2^+ \leftrightarrow PuO_2^{2+} + e^-$	–(15.82 ± 0.09) [a]
$PuO_2(am,hyd) \leftrightarrow PuO_2^+ + e^-$	–(19.78 ± 0.09) [a]
Solubility and hydrolysis of Pu(III)	
$Pu(OH)_3(am) \leftrightarrow Pu^{3+} + 3\ OH^-$	–(26.2 ± 1.5) [b c]
$Pu^{3+} + OH^- \leftrightarrow Pu(OH)^{2+}$	(7.1 ± 0.3) [a d]
$Pu^{3+} + 2\ OH^- \leftrightarrow Pu(OH)_2^+$	(12.9 ± 0.7) [a d]
$Pu^{3+} + 3\ OH^- \leftrightarrow Pu(OH)_3^0(aq)$	(15.8 ± 0.5) [a d]
Solubility and hydrolysis of Pu(IV)	
$PuO_2(am, hyd) \leftrightarrow Pu^{4+} + 4\ OH^-$	–(58.33 ± 0.52) [a]
$PuO_2(cry) \leftrightarrow Pu^{4+} + 4\ OH^-$	–(64.03 ± 0.51) [a]
$Pu^{4+} + OH^- \leftrightarrow Pu(OH)^{3+}$	(14.6 ± 0.2) [a]
$Pu^{4+} + 2\ OH^- \leftrightarrow Pu(OH)_2^{2+}$	(28.6 ± 0.3) [a]
$Pu^{4+} + 3\ OH^- \leftrightarrow Pu(OH)_3^+$	(39.7 ± 0.4) [a]
$Pu^{4+} + 4\ OH^- \leftrightarrow Pu(OH)_4^0(aq)$	(47.5 ± 0.5) [a]
Solubility and hydrolysis of Pu(V)	
$PuO_2OH(am) \leftrightarrow PuO_2^+ + OH^-$	–(9.0 ± 0.5) [a]
$PuO_{2.5}(s,hyd) \leftrightarrow PuO_2^+ + OH^-$	–(14.0 ± 0.5) [a]
$PuO_2^+ + OH^- \leftrightarrow PuO_2OH^0(aq)$	(2.7 ± 0.7) [a e]
$PuO_2^+ + 2\ OH^- \leftrightarrow PuO_2(OH)_2^-$	(4.4 ± 0.5) [a e]
Solubility and hydrolysis of Pu(VI)	
$PuO_2(OH)_2{\cdot}H_2O(s) \leftrightarrow PuO_2^{2+} + 2\ OH^- + H_2O(l)$	–(22.5 ± 1.0) [a]
$PuO_2^{2+} + OH^- \leftrightarrow PuO_2(OH)^+$	(8.5 ± 0.5) [a]
$PuO_2^{2+} + 2\ OH^- \leftrightarrow PuO_2(OH)_2^0(aq)$	(14.8 ± 1.5) [a]
$PuO_2^{2+} + 3\ OH^- \leftrightarrow PuO_2(OH)_3^-$	(21.7 ± 0.4) [a]
$2\ PuO_2^{2+} + 2\ OH^- \leftrightarrow (PuO_2)_2(OH)_2^{2+}$	(20.5 ± 1.0) [a]

[a] Adapted from Neck et al. (2007) and Guillaumont et al. (2003).
[b] Taken from Guillaumont et al. (2003).
[c] Value is originally reported in Felmy et al. (1989), but with an assigned uncertainty of ± 0.8 in log_{10}-units.
[d] In analogy with Am(III).
[e] In analogy with Np(V).

Table A2
SIT ion interaction coefficients for Pu aqueous species in NaCl solutions.

I	j	ε_{ij} (kg·mol^{-1})	Reference
H^+	Cl^-	0.12 ± 0.01	(Guillaumont et al., 2003)
Na^+	Cl^-	0.03 ± 0.01	(Guillaumont et al., 2003)
Na^+	OH^-	0.04 ± 0.01	(Guillaumont et al., 2003)
Pu^{3+}	Cl^-	0.23 ± 0.02	(Neck et al., 2009)
$Pu(OH)^{2+}$	Cl^-	−0.04 ± 0.07	(Neck et al., 2009)
$Pu(OH)_2^{+}$	Cl^-	−0.06 ± 0.08	(Neck et al., 2009)
$Pu(OH)_3^0$(aq)	Cl^-	0.00	[a]
$Pu(OH)_3^0$(aq)	Na^+	−0.17 ± 0.10	(Neck et al., 2009)
Pu^{4+}	Cl^-	0.4 ± 0.1	(Neck and Kim, 2001)
$PuOH^{3+}$	Cl^-	0.2 ± 0.1	(Neck and Kim, 2001)
$Pu(OH)_2^{2+}$	Cl^-	0.1 ± 0.1	(Neck and Kim, 2001)
$Pu(OH)_3^{+}$	Cl^-	0.05 ± 0.1	(Neck and Kim, 2001)
$Pu(OH)_4^0$(aq)	Na^+/Cl^-	0.00	[a]
PuO_2^{+}	Cl^-	0.09 ± 0.05[b]	(Guillaumont et al., 2003)
PuO_2OH(aq)	Na^+/Cl^-	0.00	[a]
$PuO_2(OH)_2^-$	Na^+	−0.01 ± 0.07 [b]	(Guillaumont et al., 2003)
PuO_2^{2+}	Cl^-	0.21 ± 0.02 [c]	(Guillaumont et al., 2003)
PuO_2OH^+	Cl^-	0.05 ± 0.1 [c]	(Hummel, 2009)
$PuO_2(OH)_2$(aq)	Na^+/Cl^-	0.00	[a]
$PuO_2(OH)_3^-$	Na^+	−0.09 ± 0.05 [d]	(Gaona et al., 2013)
$(PuO_2)_2(OH)_2^{2+}$	Cl^-	0.69 ± 0.07 [c]	(Guillaumont et al., 2003)

[a] By definition in SIT.
[b] In analogy with Np(V).
[c] In analogy with U(VI).
[d] In analogy with Np(VI).

Appendix A. Supplementary data

Supplementary data related to this article can be found at https://doi.org/10.1016/j.apgeochem.2018.04.014.

References

Ahlrichs, R., Furche, F., Grimme, S., 2000. Comment on "Assessment of exchange correlation functionals". Chem. Phys. Lett. 325 (1–3), 317–321.

Ahlrichs, R., Furche, F., Hättig, C., Klopper, W.M., Sierka, M., Weigend, F., 2015. TURBOMOLE v7.0. University of Karlsruhe and Forschungszentrum Karlsruhe GmbH, Karlsruhe, Germany.

Allard, S., Ekberg, C., Jolsterå, R., Knutsson, A., Ödegaard-Jensen, A., 2008. Complexation of americium with a-D-isosaccharinate. In: International Solvent Extraction Conference: Fundamentals to Industrial Applications (ISEC 2008). International Atomic Energy Agency/International Nuclear Information System, Tucson, Arizona, U.S.A, pp. 1133–1138.

Almond, M., Belton, D., Humphreys, P.N., Laws, A.P., 2016. A study of the metal binding capacity of saccharinic acids formed during the alkali catalysed decomposition of cellulosic materials: nickel complexation by glucoisosaccharinic acids and xyloisosaccharinic acids. Carbohydr. Res. 427, 48–54.

Altmaier, M., Gaona, X., Fellhauer, D., Buckau, G., 2010. Intercomparison of Redox Determination Methods on Designed and Near-natural Aqueous Systems. KIT Scientific Reports 7572. (Karlsruhe, Germany).

Altmaier, M., Metz, V., Neck, V., Müller, R., Fanghänel, T., 2003. Solid-liquid equilibria of Mg(OH)2(cr) and Mg2(OH)3Cl·4H2O(cr) in the system Mg-Na-H-OH-Cl-H2O at 25°C. Geochem. Cosmochim. Acta 67, 3595–3601.

Altmaier, M., Neck, V., Müller, R., Fanghänel, T., 2005. Solubility of ThO2·xH2O(am) in carbonate solution and the formation of ternary Th(IV) hydroxide-carbonate complexes. Radiochim. Acta 93, 83–92.

Ankudinov, A.L., Ravel, B., Rehr, J.J., Conradson, S.D., 1998. Realspace multiple-scattering calculation and interpretation of X-ray absorption near-edge structure. Phys. Rev. B 58, 7565–7576.

Aspinall, G., Carter, M., Loss, M., 1956. The degradation of Xylobiose and Xylotriose by alkali. J. Chem. Soc.s, Chem. Commun. 4807–4810.

Banik, N.L., Brendebach, B., Marquardt, C.M., 2014. Investigations of actinides in the context of final disposal of high-level radioactive waste: trivalent actinides in aqueous solution. J. Radioanal. Nucl. Chem. 300, 177–183.

Birjkumar, K.H., Bryan, N.D., Kaltsoyannis, N., 2012. Is gluconate a good model for isosaccharinate in uranyl(VI) chemistry? A DFT study. Dalton Trans. 41, 5542–5552.

Bradbury, M.H., Van Loon, L.R., 1997. Cementitious Near-field Sorption Data Bases for Performance Assessment of a L/ILW Repository in a Palfris Marl Host Rock. Paul Scherrer Institute, Switzerland.

Brendebach, B., Banik, N.L., Marquardt, C.M., Rothe, J., Denecke, M., Geckeis, H., 2009. X-ray absorption spectroscopic study of trivalent and tetravalent actinides in solution at varying pH values. Radiochim. Acta 97, 701–708.

Cho, H.R., Youn, Y.S., Jung, E.C., Cha, W., 2016. Hydrolysis of trivalent plutonium and solubility of Pu(OH)3 (am) under electrolytic reducing conditions. Dalton Trans. 45, 19449–19457.

Ciavatta, L., 1980. The specific interaction theory in evaluating ionic equilibria. Ann. Chim. 70, 551–567.

Colàs, E., 2014. Complexation of Th(IV) and U(VI) by Polyhydroxy and Polyamino Carboxylic Acids. Universitat Politècnica de Catalunya (UPC), Barcelona, Spain.

De Nolf, W., Vanmeert, F., Janssens, K., 2014. XRDUA: crystalline phase distribution maps by two-dimensional scanning and tomographic (micro) X-ray powder diffraction. J. Appl. Crystallogr. 47, 1107–1117.

Deglmann, P., May, K., Furche, F., Ahlrichs, R., 2004. Nuclear second analytical derivative calculations using auxiliary basis set expansions. Chem. Phys. Lett. 384, 103–107.

Eichkorn, K., Treutler, O., Öhm, H., Ahlrichs, H.M., Ahlrichs, R., 1995. Auxiliary basis sets to approximate Coulomb potentials. Chem. Phys. Lett. 242, 652–660.

Eichkorn, K., Weigend, F., Treutler, O., Ahlrichs, R., 1997. Auxiliary basis sets for main row atoms and transition metals and their use to approximate coulomb potentials. Theor. Chem. Acc 97, 119–124.

Evans, N., 2003. Studies on Metal A-Isosaccharinic Acid Complexes. Loughborough University, Loughborough, UK.
Felmy, A.R., Cho, H., Dixon, D.A., Xia, Y., Hess, N.J., Wang, Z., 2006. The aqueous complexation of thorium with citrate under neutral to basic conditions. Radiochim. Acta 94.
Felmy, A.R., Rai, D., Schramke, J.A., Ryan, J.L., 1989. The solubility of plutionium hydroxide in dilute solution and in high-ionic-strenght cloride brines. Radiochim. Acta 48, 29–35.
Frohlich, D.R., Trumm, M., Skerencak-Frech, A., Panak, P.J., 2016. The complexation of Cm(III) with succinate studied by time-resolved laser fluorescence spectroscopy and quantum chemical calculations. Inorg. Chem. 55, 4504–4511.
Gakhokidze, R.A., 1980. Saccharinic acids. Russ. Chem. Rev. 49, 420–447.
Gamsjäger, H., Gajda, T., Sangster, J., Saxena, S.K., Voigt, W., 2012. Chemical Thermodynamics of Tin. Elsevier, North Holland, Amesterdam.
Gaona, X., Fellhauer, D., Altmaier, M., 2013. Thermodynamic description of Np(VI) solubility, hydrolysis, and redox behavior in dilute to concentrated alkaline NaCl solutions. Pure Appl. Chem. 85, 2027–2049.
Gaona, X., Montoya, V., Colàs, E., Grivé, M., Duro, L., 2008. Review of the complexation of tetravalent actinides by ISA and gluconate under alkaline to hyperalkaline conditions. J. Contam. Hydrol. 102, 217–227.
Gaona, X., Tits, J., Dardenne, K., Liu, X., Rothe, J., Denecke, M.A., Wieland, E., Altmaier, M., 2012. Spectroscopic investigations of Np(V/VI) redox speciation in hyperalkaline TMA-(OH, Cl) solutions. Radiochim. Acta 100, 759–770.
Glaus, M.A., Van Loon, L.R., 2008. Degradation of cellulose under alkaline conditions: new insights from a 12 years degradation study. Environ. Sci. Technol. 42, 2906–2911.
Glaus, M.A., Van Loon, L.R., Achatz, S., Chodura, A., Fischer, K., 1999. Degradation of cellulosic materials under the alkaline conditions of a cementitious repository for low and intermediate level radioactive waste. Part I: identification of degradation products. Anal. Chim. Acta 398, 111–112.
González-Siso, M.R., Gaona, X., Duro, L., Altmaier, M., Bruno, J., 2018. Thermodynamic model of Ni(II) solubility, hydrolysis and complex formation with ISA. Radiochim. Acta 106 (1), 31–45.
Greenfield, B.F., Holtom, G.J., Hurdus, M.H., O'Kelly, N., Pilkington, N.J., Rosevear, A., Spindler, M.W., Williams, S.J., 1995. The identification and degradation of isosaccharinic acid, a cellulose degradation product. Mater. Res. Soc. Symp. Proc. 353, 1151–1158.
Greenfield, B.F., Hurdus, M.H., Spindler, M.W., Thomason, H.P., 1997. The Effect of the Products from the Anaerobic Degradation of Cellulose on the Solubility and Sorption of Radioelements in the Near Field. Nuclear Industry Radioactive Waste Executive (Nirex), UK.
Guillaumont, R., Fanghänel, T., Neck, V., Fuger, J., Palmer, D.A., Grenthe, I., Rand, M.H., 2003. Update on the Chemical Thermodynamics of Uranium, Neptunium, Plutonium, Americium and Technetium. Elsevier, North Holland, Amesterdam.
Hohenberg, P., Kohn, W., 1964. Inhomogeneous electron gas. Phys. Rev. 136, B864–B871.
Hummel, W., 2009. Ionic Strength Corrections and Estimation of SIT Ion Interaction Coefficients, PSI Technical Report. Paul Scherrer Institut, Villigen, Switzerland.
Hummel, W., Anderegg, G., Rao, L., Puigdomenech, I., Tochiyama, O., 2005. Chemical Thermodynamics of Compounds and Complexes of U, Np, Pu, Am, Tc, Se, Ni and Zr with Selected Organic Ligands. Elsevier, North-Holland, Amsterdam.
Keith-Roach, M., Lindgren, M., Källström, K., 2014. Assessment of Complexing Agent Concentrations in SFR. Swedish Nuclear Fuel and Waste Management Co, Stockholm, Sweden.
Kinniburgh, D.G., Cooper, D.M., 2009. PhreePlot: Creating Graphical Output with PHREEQC. Centre for Ecology and Hydrology, Deiniol Road, Bangor, Gwynedd, LL57 2UW, UK.
Klamt, A., 1995. Conductor-like screening model for real solvents: a new approach to the quantitative calculation of solvation phenomena. J. Phys. Chem. 99, 2224–2235.
Klamt, A., Schuurmann, G., 1997. Chem Soc Perkin Trans 2 1993 (5) 799;(b) Baldridge, K.; Klamt. A. J Chem Phys 106, 6622.
Kobayashi, T., Sasaki, T., Kitamura, A., 2017a. In: Thermodynamic Study on the Complexation of U(IV) with Isosaccharinic Acid, Actinides Conference, Book of Abstracts, Sendai, pp. 78.
Kobayashi, T., Teshima, T., Sasaki, T., Kitamura, A., 2017b. Thermodynamic model for Zr solubility in the presence of gluconic acid and isosaccharinic acid. J. Nucl. Sci. Technol. 54, 233–241.
Kohn, W., Sham, L.J., 1965. Self-consistent equations including exchange and correlation effects. Phys. Rev. 140, A1133–A1138.
Moreton, A.D., 1993. Thermodynamic modeling of the effect of hydroxycarboxylic acids on the solubility of plutonium at high pH. Mater. Res. Soc. Symp. Proc. 294, 753–758.
Moreton, A.D., Pilkington, N.J., Tweed, C.J., 2000. Thermodynamic Modeling of the Effect of Hydroxycarboxylic Acids on the Solubility of Plutonium at High PH. Nuclear Industry Radioactive Waste Executive (Nirex), UK.
Moritz, A., Cao, X., Dolg, M., 2006. Quasirelativistic energy-consistent 5f-in-core pseudopotentials for trivalent actinide elements. Theoretical Chemistry Accounts 117, 473–481.
Moritz, A., Cao, X., Dolg, M., 2007. Quasirelativistic energy-consistent 5f-in-core pseudopotentials for divalent and tetravalent actinide elements. Theoretical Chemistry Accounts 118, 845–854.
Neck, V., Altmaier, M., Fanghänel, T., 2007. Solubility of plutonium hydroxides/hydrous oxides under reducing conditions and in the presence of oxygen. Compt. Rendus Chem. 10, 959–977.
Neck, V., Altmaier, M., Rabung, T., Lützenkirchen, J., Fanghänel, T., 2009. Thermodynamics of trivalent actinides and neodymium in NaCl, MgCl2, and CaCl2 solutions: solubility, hydrolysis, and ternary Ca-M(III)-OH complexes. Pure Appl. Chem. 81, 1555–1568.
Neck, V., Kim, J.I., 2001. Solubility and hydrolysis of tetravalent actinides. Radiochim. Acta 89, 1–16.
Nelder, J.A., Mead, R., 1965. A simplex method for function minimization. Comput. J. 7, 308.
Parkhurst, D.L., Appelo, C.A.J., 1999. User's Guide to PHREEQC (Version 2) – a Computer Program for Speciation, Batch Reaction, One-dimensional Transport and Inverse Geochemical Calculation, Water-resources Investigation Report 99–4259. USGS, Denver, Colorado, USA, pp. 312.
Parkhurst, D.L., Appelo, C.A.J., 2013. Description of Input and Examples for PHREEQC Version 3—A Computer Program for Speciation, Batch-reaction, One-dimensional Transport, and Inverse Geochemical Calculations: U.S. Geological Survey Techniques and Methods. available only at http://pubs.usgs.gov/tm/06/a43/.
Pavasars, I., Hagberg, J., Borén, H., Allard, B., 2003. Alkaline degradation of cellulose: mechanisms and kinetics. J. Polym. Environ. 11, 39–47.
Powell, M.J.D., 1965. A method for minimizing a sum of squares of non-linear functions without calculating derivatives. Comput. J. 7, 303–307.
Rai, D., Hess, N.J., Xia, Y.X., Rao, L., Cho, H.M., Moore, R.C., Van Loon, L.R., 2003. Comprehensive thermodynamic model applicable to highly acidic to basic conditions for isosaccharinate reactions with Ca(II) and Np(IV). J. Solut. Chem. 32, 665–689.
Rai, D., Kitamura, A., 2017. Thermodynamic equilibrium constants for important isosaccharinate reactions: a review. J. Chem. Therm. 114, 135–143.
Rai, D., Rao, L., Moore, D.A., 1998. The influence of isosaccharinic acid on the solubility of Np(IV) hydrous oxide. Radiochim. Acta 83, 9–13.
Rai, D., Rao, L., Moore, R.C., Bontchev, R., Holt, K., 2004. Development of Biodegradable Isosaccharinate-containing Foams for Decontamination of Actinides: Thermodynamic and Kinetic Reactions between Isosaccharinate and Actinides on Metal and Concrete Surfaces. USDOE Office of Science, United States of America Technical Report.
Rai, D., Yui, M., Moore, D.A., Rao, L., 2009. Thermodynamic model for ThO2(am) solubility in isosaccharinate solutions. J. Solut. Chem. 38, 1573–1587.
Randall, M., Rigby, B., Thomson, O., Trivedi, D., 2013. Assessment of the Effects of Cellulose Degradation Products on the Behaviour of Europium and Thorium. National Nuclear Laboratory. Chadwick House, Warington, UK.
Ravel, B., Newville, M., 2005. ATHENA, ARTEMIS, HEPHAESTUS: data analysis for X-ray absorption spectroscopy using IFEFFIT. J. Synchrotron Radiat. 12, 537–541.
Rothe, J., Butorin, S., Dardenne, K., Denecke, M.A., Kienzler, B., Loble, M., Metz, V., Seibert, A., Steppert, M., Vitova, T., Walther, C., Geckeis, H., 2012. The INE-Beamline for actinide science at ANKA. Rev. Sci. Instrum. 83, 043105.
Rothe, J., Walther, C., Denecke, M., Fanghaenel, T., 2004. XAFS and LIBD investigation of the formation and structure of colloidal Pu(IV) hydrolysis products. Inorg. Chem. 43, 4708–4718.
Schäfer, A., Horn, H., Ahlrichs, R., 1992. Fully optimized contracted Gaussian basis sets for atoms Li to Kr. J. Chem. Phys. 97, 2571–2577.
SKB, 2008. Safety Analysis SFR 1. Long-term Safety. Svensk Kärnbränslehantering AB. (Stockholm, Sweden).
Skerencak-Frech, A., Maiwald, M., Trumm, M., Froehlich, D.R., Panak, P.J., 2015. The complexation of Cm(III) with oxalate in aqueous solution at T = 20-90 degrees C: a combined TRLFS and quantum chemical study. Inorg. Chem. 54, 1860–1868.
Smrcok, L., 1989. Rietveld refinement of Y2O3, using the pearson VII profile shape function. Cryst. Res. Technol. 24, 607–611.
Stern, E.A., Newville, M., Ravel, B., Yacoby, Y., Haskel, D., 1995. The UWXAFS analysis package – philosophy and details. Physica B 209, 117–120.
Tasi, A., Gaona, X., Fellhauer, D., Böttle, M., Rothe, J., Dardenne, K., Schild, D., Grive, M., Colas, E., Bruno, J., Kallstrom, K., Altmaier, M., Geckeis, H., 2018. Redox behavior and solubility of Plutonium under alkaline, reducing conditions. Radiochim. Acta 106 (4), 259–279. https://doi.org/10.1515/ract-2017-2870.
Tits, J., Wieland, E., Bradbury, M.H., 2005. The effect of isosaccharinic acid and gluconic acid on the retention of Eu(III), Am(III) and Th(IV) by calcite. Appl. Geochem. 20, 2082–2096.
Tits, J., Wieland, E., Bradbury, M.H., Eckert, P., Schaible, A., 2002. The Uptake of Eu(III) and Th(IV) by Calcite under Hyperalkaline Conditions. Paul Scherrer Insitut, Villigen, Switzerland.
Treutler, O., Ahlrichs, R., 1995. Efficient molecular numerical integration schemes. J. Chem. Phys. 102, 346–354.
Van Loon, L.R., Glaus, M.A., 1998. Experimental and Theoretical Studies on Alkaline Degradation of Cellulose and its Impact on the Sorption of Radionuclides. Paul Scherrer Institute, Switzerland.
Van Loon, L.R., Glaus, M.A., Laube, A., Stallone, S., 1999. Degradation of cellulosic materials under the alkaline conditions of a cementitious repository for low- and intermediate-level radioactive waste: II. Degradation kinetics. J. Environ. Polym. Degrad. 41–51.
Vercammen, K., 2000. Complexation of Calcium, Thorium and Europium by A-Isosaccharinic Acid under Alkaline Conditions. Swiss Federal Institute of Technology, Zurich, Switzerland.
Vercammen, K., Glaus, M.A., Van Loon, L.R., 1999. Evidences for the existence of complexes between Th(IV) and α-isosaccharinic acid under alkaline conditions. Radiochim. Acta 84, 221–224.
Vercammen, K., Glaus, M.A., Van Loon, L.R., 2001. Complexation of Th(IV) and Eu(III) by alpha-isosaccharinic acid under alkaline conditions. Radiochim. Acta 89, 393–401.
von Arnim, M., Ahlrichs, R., 1999. Geometry optimization in generalized natural internal coordinates. J. Chem. Phys. 111, 9183–9190.
Walther, C., Rothe, J., Brendebach, B., Fuss, M., Altmaier, M., Marquardt, C.M., Büchner, S., Cho, H.-R., Yun, J.I., Seibert, A., 2009. New insights in the formation processes of Pu(IV) colloids. Radiochim. Acta 97, 199–207.
Warwick, P., Evans, N., Hall, T., Vines, S., 2004. Stability constants of uranium(IV)-α-isosaccharinic acid and gluconic acid complexes. Radiochim. Acta 92, 897–902.
Wong-Ng, W., McMurdie, H.F., Hubbard, C.R., M, A.D., 2001. JCPDS-icdd research associateship (cooperative program with NBS/NIST). Journal of Research of the National Institute of Standards and Technology 106, 1013–1028.
Zachariansen, W.H., 1949. Crystal chemical studies of the 5f-series of elements. Xii. New compounds representing known structure types. Acta Crystallogr. 2, 388–390.
Zhang, Z., Helms, G., Clark, S.B., Tian, G., Zanonato, P., Rao, L., 2009. Complexation of uranium(VI) by gluconate in acidic solutions: a thermodynamic study with structural analysis. Inorg. Chem. 3814–3824.